STRUCTURAL ANALYSIS OF ROTAVIRUS ANTIGEN – ANTIBODY INTERACTIONS

By

Mohammed Sefiu Aiyegbo

Dissertation submitted to the

Faculty of the Graduate School of Vanderbilt University

in partial fulfillment of the requirements for the degree of

DOCTOR OF PHILOSOPHY

in

Microbiology and Immunology

May 2013

Nashville, Tennessee

Approved:

James W. Thomas

Terence Dermody

Benjamin Spiller

Phoebe Stewart

James E. Crowe, Jr.

To the memory of my mother and father:

Good, better, best
I shall never rest
Until my good is better
And my better, best

I miss you dearly

ACKNOWLEDGEMENTS

I am hugely indebted to many people that have contributed to the success of this research work. It is with immense gratitude that I acknowledge the support and assistance of my advisor, James E. Crowe, Jr., and the past and present members of the Crowe laboratory. Jim allowed me the freedom to explore on my own, and his enthusiasm for science has helped to surmount the many obstacles along the way. I will cherish the late night emails and the other interests we have shared throughout the course of my graduate studies. I cannot find words to express my heartfelt gratitude to Frances Smith-House, our lab manager, mom and guiding light for her support over the years. I would like to thank my collaborators: the laboratories of Benjamin Spiller and Jens Meiler at Vanderbilt University, Phoebe Stewart at Case Western Reserve University and the now-deceased Virgil Woods at University of California, San Diego. I would also like to thank all the students I have worked with, particularly Ilyas Eli, who contributed to the data presented in this dissertation.

For their consistent guidance, insight, and excellent ideas, I would like to express my deepest appreciation to my dissertation committee: James W. (Tom) Thomas (Chair), Terence Dermody, Benjamin Spiller and Phoebe Stewart. My sincere thanks to the Vanderbilt BRET Office, the Department of Pathology, Microbiology and Immunology and the Division of Pediatric Infectious Diseases for their support. NIH funding, R01 AI-57933 and R21 AI-083574, provided financial support for this work.

Finally, I must acknowledge my family who has provided steadfast support, love and patience; and encouraged me throughout this endeavor. To my numerous friends,

who have become my extended family, I am thankful for your kindness, generosity and the laughter we have shared. Special thanks to Sainabou, for her unwavering support and her sometimes not-so-gentle encouragement. I could always count on you for that extra push I needed. And to Gerren: I will forever be grateful for your love, patience, concern, support and strength all these years. Sir Isaac Newton once wrote, “If I have seen a little further, it is by standing on the shoulders of giants.” You are all, my giants.

TABLE OF CONTENTS

LIST OF TABLES

LIST OF FIGURES

LIST OF ABBREVIATIONS

Ab	antibody
Ag	antigen
ARE	apical recycling endosome
ATCC	American type culture connection
CCD	charged-coupled device
cDNA	complementary deoxyribonucleic acid
CDR	complementarity determining region
C_H	constant heavy chain
C_L	constant light chain
CMV	cucumber mosaic virus
Cryo-EM	cryo-electron microscopy
CTF	contrast transfer function
DLP	double-layered particle
DNA	deoxyribonucleic acid
dsRNA	double stranded ribonucleic acid
DXMS	hydrogen-deuterium exchange mass spectroscopy
EGTA	ethylene glycol tetraacetic acid
EDTA	ethylene diamine tetraacetic acid
EM	electron microscopy
Fab	fragment antigen binding
FBS	fetal bovine serum

FEG	field emission gun
FSC	Fourier shell correlation
gp120	glycoprotein 120
gp140	glycoprotein 140
HCDR2	hypervariable complementarity-determining region 2 of the heavy chain
HIV-1	human immunodeficiency virus type 1
IgA	immunoglobulin A
IM	infection medium
IPTG	isopropyl β-D-1-thiogalactopyranoside
kDa	kilo Dalton
L	litre
LB	Luria broth
nt	nucleotide
mAb	monoclonal antibody
MEM	minimum essential medium
mM	milli Molar
MOI	multiplicity of infection
mRNA	messenger ribonucleic acid
PCR	polymerase chain reaction
PDB	protein data bank
PEG	polyethylene glycol
pfu	plaque forming unit
pIgA	polymeric immunoglobulin A
RNA	ribonucleic acid

RV	rotavirus
RRV	rhesus rotavirus
SCID	severe combined immunodeficiency
SDS-PAGE	sodium dodecyl sulfate polyacrylamide gel electrophoresis
SIV-1	simian immunodeficiency virus type 1
TEM	transmission electron microscopy
TLP	triple-layered particle
TLS	translation/libration/screw
V_H	variable heavy chain
V_L	variable light chain
VP1	viral protein 1
VP2	viral protein 2
VP3	viral protein 3
VP4	viral protein 4
VP5	viral protein 5
VP6	viral protein 6
VP6hd	viral protein 6 head domain
VP7	viral protein 7
VP8	viral protein 8

CHAPTER I

INTRODUCTION

Rotavirus gastroenteritis

Rotaviruses, double-stranded RNA viruses that belong to the *Reoviridae* family, are the major causative agents for acute gastroenteritis in infants and young children worldwide (17). Almost all children are infected with rotavirus (RV) by age 5, and infection results in an estimated half million deaths each year in children younger than 5 years of age (28). Following initial infections, most children show robust immune responses to RV. Rotavirus induced gastroenteritis symptoms are fever, watery stool, and vomiting lasting for about 4-7 days with the severity ranging from loose stools to death. These outcomes are dependent mostly on the quality of medical intervention available and access to oral replacement of fluids and electrolytes.

Rotavirus biology

All vertebrates have their own species-specific rotavirus. Rotaviruses have multi-shelled non-enveloped icosahedrally symmetric capsids of ~ 100 nm diameter. The RV genome consists of 11 segments of double-stranded RNA that each code for a single protein, with the exception of segment 11 that codes for two proteins. Of the 12 polypeptides produced by the rotavirus genome, six are structural and six are non-structural. The virions are non-enveloped, triple-layered, icosahedral viruses. The triple-layered particle (TLP) is composed of an inner capsid layer of virus protein 2 (VP2), an intermediate capsid layer

of VP6, and an outer capsid layer made up of VP7 and spikes of VP4 protein (Figure 1-1) (18, 52, 53, 76, 78). VP7 is a glycoprotein, and VP4 is proteolyzed into VP8 and VP5. These modifications of the outer capsid proteins are referred to as the G and P proteins in serotype nomenclature of rotavirus, which is based on the combinations of G and P type proteins present in the outer capsid, that determine their antigenicity. Because of the segmented nature of the RV genome, reassortment of the outer capsid proteins is quite common in nature and leads to a diversity of serotypes. The intermediate and outer capsid layers both have a T=13 *l* icosahedral symmetry that defines 132 channels within the viral architecture into three types based on their position with respect to the T=13 icosahedral symmetry axis (41, 52, 57, 61, 75). There are 12 type I channels, located at the icosahedral five-fold axes, that have narrow openings through which nascent viral mRNA egresses out of the particle during viral transcription (53). The type II channels located at the quasi-six-fold axes directly adjacent to the type I channels have larger openings than the type I channels. The type III channels also have larger openings than the type I channels and are located at the quasi-six-fold axes not directly adjacent to the type I channels and close to the icosahedral three-fold axes. Rotavirus, in its TLP form, is transcriptionally-inactive; the double-layered particle (DLP) is transcriptionally-active (4, 12, 56, 78). The viral transcription machinery, composed of VP1 and VP3, is located near the icosahedral five-fold axis below the VP2 layer (53). Upon cell entry, the outer layer is lost leaving a "double-layered particle" (DLP). It is the DLP structure that is the transcriptionally active form of the virus. Mature TLPs are capable of initiating transcription but are unable to elongate the nascent transcripts beyond 6-7 nt in length (34). The dsRNA molecules bound to the central core protein VP2 as well as the viral

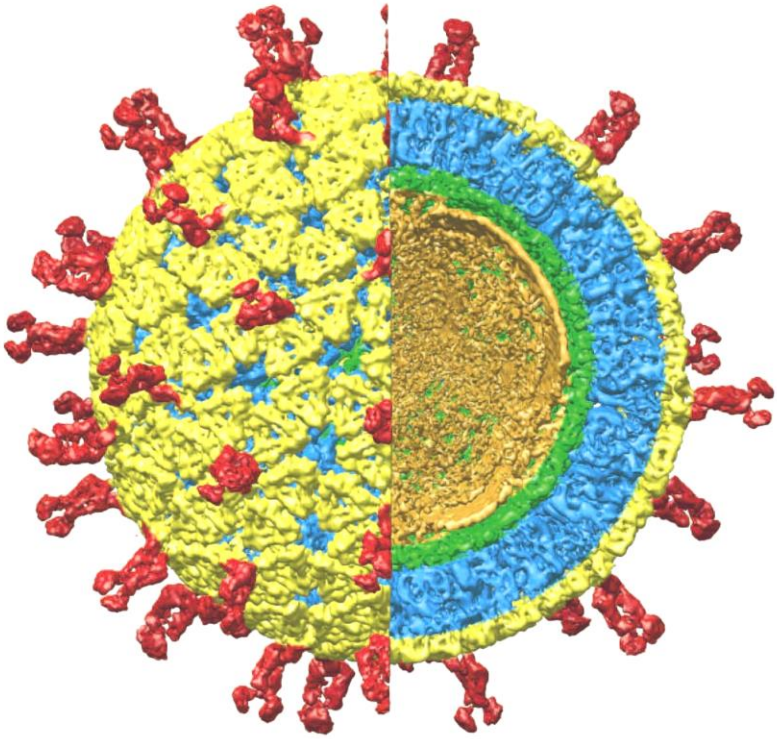

1-1. Rotavirus at 9.5 Å resolution. The major capsid components are color coded with the right side of the structure cropped to reveal the three stratified layers. Red = VP4, Yellow = VP7, Blue = VP6, Green = VP2, central cavity is dsRNA core. (38)

RNA-dependent RNA polymerase VP1 and VP3 are transcribed in the cytoplasm upon cell entry and extruded from the viral five-fold axis (35). The intermediate layer surrounding the inner core is composed of VP6, which is the most antigenic RV protein in humans but does not induce classically neutralizing antibodies because it is masked by the outer capsid proteins VP4 and VP7. Indeed, VP4 and VP7 induce the classical neutralizing antibodies associated with protection *in vivo* from cell entry. However, some anti-VP6 IgA mAbs protect mice from infection and clear chronic infections in immuno-compromised SCID mice (10). The mechanism of this neutralization is not fully understood, but is assumed to target the transcription step of the virus lifecycle. This is based on a dose-dependent block of viral transcription by these anti-VP6 mAbs when introduced to cells concurrently with DLPs (20). The role of these antibodies in resolving human infection is unclear, but studies show a large fraction of naïve B cells from both adults and neonates interact with VP6 (27), suggesting VP6 is an important endogenous target for the adaptive immune system for blocking viral secondary infection. VP6 of all group A rotaviruses share a high degree of antigenic cross-reactivity and could potentially be responsible for heterotypic protection observed following primary rotavirus infections. Given the segmented nature of the rotavirus genome, diversity of the outer capsid is quite high due to reassortment of the G and P proteins during viral assembly and RNA packaging (62). Although this has allowed for selection of human serotypes that are either attenuated by reassortment with bovine rotavirus or less virulent strains for vaccine development, it also suggest vaccine development is hindered by the prevalence and distribution of worldwide seasonally changing rotavirus serotype diversity leaving uncommon or evolving serotypes unchallenged.

Functional maturation of human antibodies in response to rotavirus

A three-step process generates antibody-antigen complementarity. Initially functional antibodies must be assembled by recombination of the variable (V), diversity (D), and joining (J) segments in the heavy and light chain variable regions. This recombination process also incorporates increased diversity by nucleotide addition or subtraction at splice junctions created by the non-homologous end-joining pathway. Finally, somatic hyper-mutation of the heavy chain variable (V_H) and light chain variable (V_L) regions increases Ab-Ag affinity through B-cell proliferative selection (1). It was initially speculated that infants produce relatively poor neutralizing antibodies because of constrained or fetal like usage of V_H and V_L gene segments. However, our laboratory has shown that a bias exists toward the V_H 1-46 gene segments found in circulating B-cells is similar in both the adult and infants for B-cell repertoires that produce antibodies against rotavirus VP6 (70, 71). Rather than a constraint in gene segment usage, we and others have determined that somatic hyper-mutation of the V_H and V_L CDRs (Figure 1-2) are responsible for the increased affinity for adult versus infant antibodies to rotavirus antigen VP6 (27). Mutation analysis of the major residues differing in neutralizing, non-neutralizing and germline sequences has highlighted which are responsible for increased affinity and presumably underlies antibody neutralizing effects (27).

High affinity of binding between antigen and antibody is generally thought to be directly proportional to the antiviral activity of the antibody. Although epitope matched antibodies are rare, this statement is generally supported by the study of the RV6-26

versus RV6-25 (27), as well as additional analysis of neutralizing antibodies targeting the human immunodeficiency virus type-1 (HIV-1) envelope protein gp120. Of three clonal antibodies assessed for the effect of individual amino acid replacements on antigen affinity and HIV-1 neutralization, the highest affinity constant correlated with the greatest HIV-1 neutralizing activity (31, 39, 63, 67, 77). However, some studies have challenged the paradigm that affinity alone underlies viral lifecycle neutralization. For instance, an antibody to the glycoprotein 140 (gp140) from simian immunodeficiency virus (SIV-1) has high affinity for both SIV/17E-CL and SIV/mac239 gp140 proteins, but acts to neutralize only the SIV/17E-CL strain (64). Indeed, a panel of mAbs that had high affinity to the SIV/17E-CL strain failed to exhibit neutralizing activity. Therefore, affinity is an important determinant but maybe secondary to epitope specificity and context when it comes to neutralizing activity (55). This would suggest that neutralizing effects are derived not from maturation of affinity, but by the specific antigen epitope interaction with the antibody. This suggestion is supported by the examination of avidity of the antibody interaction on neutralization for the RV6-26 antibody, which is not a classical neutralizing antibody in that it does not block cell entry by recognizing outer capsid proteins. The multiple valencies of antibodies are thought to allow formation of multiple interactions with a single virion or virions, which are usually composed of repetitive protein subunits in their capsids. In humans, the initial antibody responses take the form of the IgM isotype with penta- or hexameric construction providing 10 to 12 epitope binding sites. This increased valency compensates for the lower affinity of the initial response. Therefore, its surprising then that the monovalent RV6-26 Fab showed similar rotavirus transcription inhibition in co-transfection assays with DLPs as did the

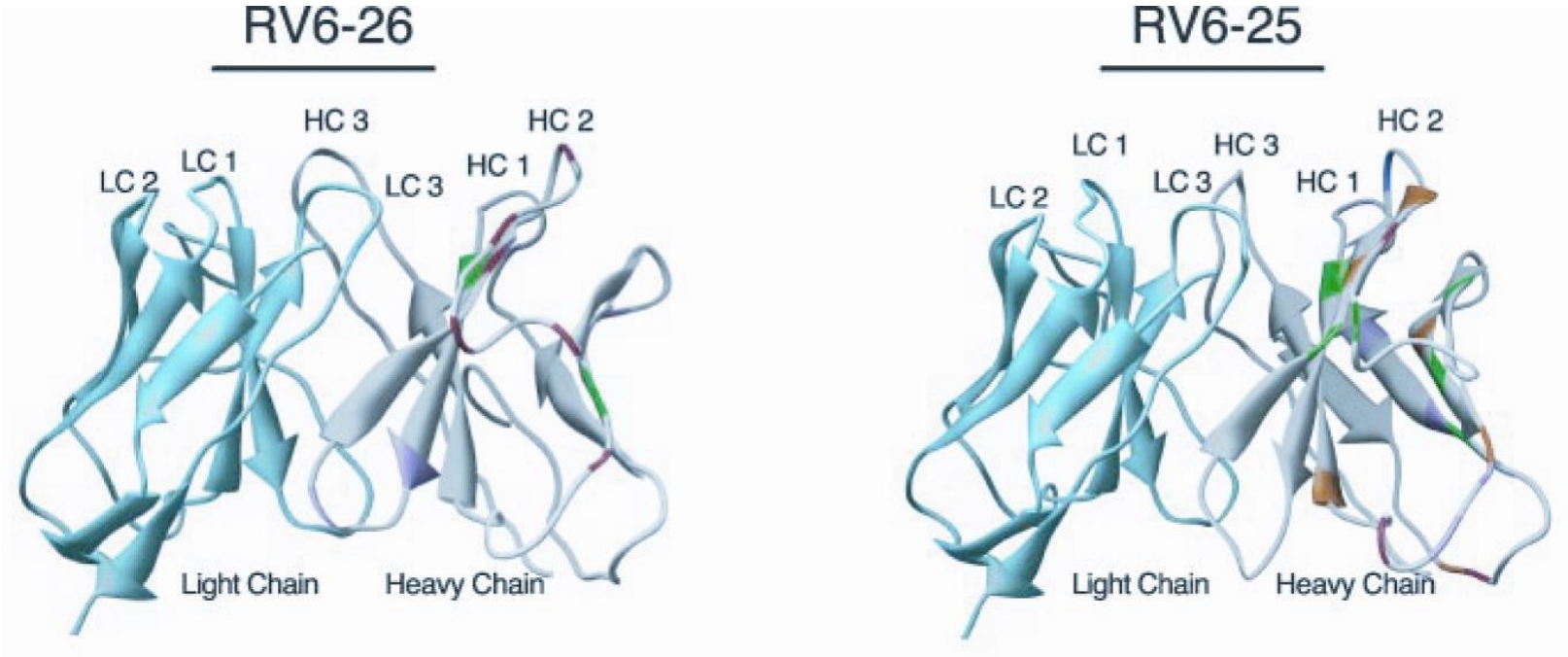

Figure 1-2. Mutational analysis of major residues differing in inhibiting, non-inhibiting or germline sequences. RV6-26 inhibiting and RV6-25 non-inhibiting antibody structures showing the CDRs of both the light and heavy chain variable regions as well as the sites of somatic mutations that resulted in affinity changes. Color scheme for the mutations are pink for no effect on affinity, red for deleterious on affinity, and green for advantageous for affinity.

potent multivalent murine IgA mAb 7D9 (20, 27). Together, these studies suggest specific residue interactions may have a direct effect on neutralizing activity and determining these Ab-Ag interactions will be critical to understanding neutralization.

Structural studies of transcriptionally inactive DLPs bound to VP6 neutralizing Abs

Multiple structures of rotavirus in complex with neutralizing antibodies have been determined. These neutralized DLPs have been shown to be transcriptionally blocked and that the DLPs generally revert to a transcriptionally inactive TLP or mature particle conformation. Comparative analysis of competent and incompetent DLP complexes bound to neutralizing and non-neutralizing complexes suggested that the type-1 pore size at the five fold axis of the T=13 icosahedral VP6 intermediate layer is reduced by 50% in complexes that were transcriptionally inactive (32). This pore size change is due to conformational changes in the VP6-VP3 interaction at this five-fold axis. The anti-VP6 IgA mAb 7D9, which protects mice from rotavirus infection and can clear rotavirus infection from immune compromised SCID mice, binds the upper spike of VP6 on the face toward VP7 boundary (20). This localization again suggests a conformation change is induced by mAb binding to the particle and may revert the DLP structure to a TLP like mature, transcriptionally inactive form. Transcriptional activity of the 7D9 inactivated DLPs mimicked TLPs in that only 6-7 nt could be transcribed and further elongation of the product was blocked (20). Although these structural studies showed conformational changes due to the neutralizing mAb interaction with the VP6 protein, neither had sufficient resolution to resolve mechanisms that underlie the transcriptional inactivation or map the interaction.

Direct visualization of the RV6-26 and RV6-25 interactions by cryo-EM has shown that the two epitope-matched antibodies bind to the rotavirus DLP differently and give different overall density patterns (27). The RV6-26 Fab molecules were centered inside each of the 132 channels created by VP6 trimer spikes on the DLP. The density attributed to the RV6-26 Fab could contain at least two Fab molecules per VP6 pore, although at the low ~22 Å resolution the exact Fab stoichiometry could not be discerned. However, the RV6-25 non-neutralizing Fab did not occupy the center of any of the 132 pores, although Fabs were observed binding to the side of VP6 similar to the RV6-26 Fab. Since transcription occurs out the type I pore of the five-fold axis of the rotavirus DLP, the neutralizing ability of the RV6-26 Fab was assigned to its obstruction of the type I pore, which was not obstructed in the RV6-25 (Figure 1-3). These lower-resolution structures solved in this study did not resolve the site of interaction between either antibody with the VP6 antigen. Instead, it was assumed due to the differences in binding patterns that the epitopes were distinct for each antibody. However, heavy chain repositioning could also account for the difference in the Fab density positions, while both antibodies could recognize the same epitope. Without higher-resolution structures, it is not possible to determine the relative contribution of the specific residue changes from the germline to the adult neutralizing and non-neutralizing antibody structure both in regard to the overall viral structure, as well as the complementarity to the VP6 epitope. Therefore, it is highly desirable to determine the nature of these Ab-Ag interactions at as near residue resolution as possible. A recent cryo-EM study of rotavirus DLPs has reached near atomic resolution, with comparable clarity in electron density maps as the 3.8 Å VP6 atomic resolution x-ray structure (79). This work was able to achieve higher

resolution compared to the above study by including 8,400 particles in the final reconstruction versus only 90 to 150 virus particles in the above-mentioned studies. In addition to using the icosahedral symmetry of the DLP, which yielded resolutions that resolved large aromatic side chains, further averaging was performed based on the VP6 subunit T=13 icosahedrally arranged trimers. This additional 13-fold averaging of the VP6 layer allowed nearly all the large side chains to be recognized in the cryo-EM electron density map. Structures for antibodies bound to the VP6 capsomers will not be averaged in such an approach, but structural changes to VP6 induced by antibody bind should be resolved by additional 13-fold averaging.

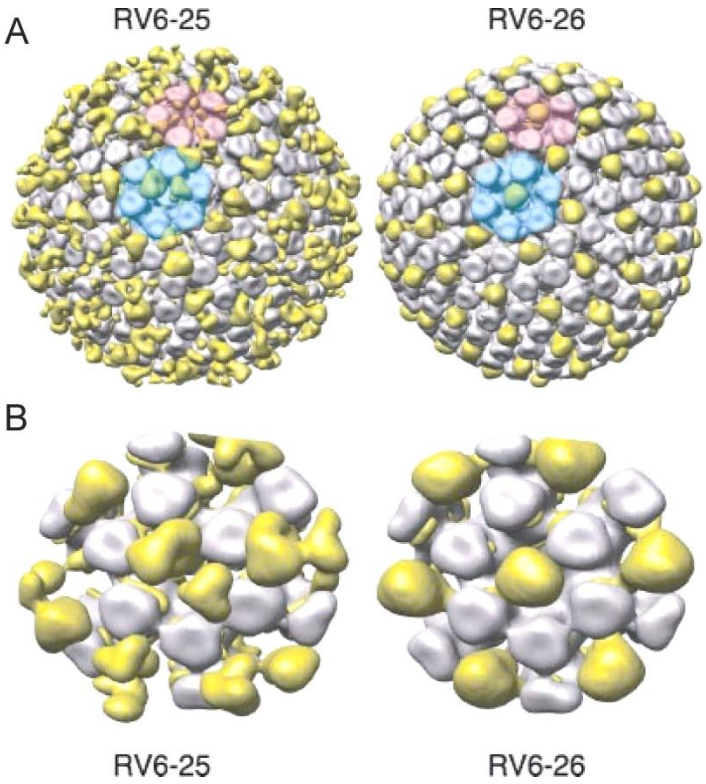

Figure 1-3: The ~22 Å cryo-EM structures of the rotavirus DLP: Fab complexes reveal different binding patterns. (A). Complete RV DLP:Fab structure with the Fab colored in yellow. The blue region highlights the five-fold symmetric type I pore where transcripts leave the DLP. (B). Closer views of the five-fold axis. (27)

Thesis overview

The experiments described in this dissertation were designed to investigate the structural basis of rotavirus antigen-antibody interactions. In chapter II, I show two high-resolution crystal structure of a rotavirus VP6 construct and RV6-26 Fab. I also define and epitope and paratope that form the basis of their interaction. In chapter III, I define the mechanism by which RV6-26 mediates its antiviral function on RV-DLP. Finally, in chapter IV, I discuss the structural basis of the inability of RV6-25 to inhibit viral transcription; Chapter V summarizes the data and offers directions for future studies.

CHAPTER II

CRYSTAL STRUCTURE OF ROTAVIRUS VP6 HEAD DOMAIN AND ANTI-VP6 FAB

Introduction

Protective and neutralizing antibodies induced in animals or humans following a rotavirus infection classically are thought to be directed against VP4 and VP7 (45, 46). However, the highest serum titers of human antibodies binding to rotavirus after infections typically are directed against VP6. Our laboratory previously identified the molecular basis for the natural human B cell response to RV VP6, comprising an antibody repertoire that is dominated by the use of a single antibody heavy chain variable gene, V_H1-46 (70). VP6-specific human antibodies encoded by V_H1-46 are the most common RV-specific antibodies in B cells made by infants and adults, including intestinal homing B cells (70-73). One such antibody, RV6-26, has a high affinity to RV VP6 and inhibits virus in an intracellular inhibition assay (27). Even though site-directed mutagenesis has identified the heavy chain complementarity-determining region 2 (HCDR2) to be driving the interaction between RV6-26 and RV VP6, the specific epitope of the RV6-26 antibody on the VP6 is unknown (27).

To determine the epitope of RV6-26, we attempted to determine the x-ray crystal structure of the RV6-26-VP6 complex. In this study, we were able to determine the structure of the VP6 head domain (VP6hd) and RV6-26 Fab separately and use

hydrogen-deuterium exchange mass spectrometry (DXMS) to determine the epitope of RV6-26.

Materials and methods

Design, expression and purification of VP6 head domain. All the x-ray crystallography studies with the VP6 head domain were performed in collaboration with Benjamin Spiller's laboratory in the Department of Pathology, Microbiology and Immunology. A DNA copy of the VP6 sequence encoding residues 147 – 339 was amplified from a full-length VP6 DNA construct (synthesized by GeneArt, Regensburg, Germany) by polymerase chain reaction (PCR) with Pfu Ultra polymerase (Stratagene) using the following primers:

Forward: 5´-GGAAGGccatggccCGGACCGGCTTCACCTTCCAC-3´

Reverse: 5´- GTGGTGctcgagGCTGGCGTCGGCCAGCACGC-3´

The PCR product was cloned into the pET28a vector (Novagen) using the NcoI and XhoI restriction sites. For expression and purification, the pET28a vector containing the head domain construct was transformed into BL21(DE3) *E. coli* strain. Cells were grown in 1 L of LB medium to an OD_{600} of 0.6 and protein expression then induced by addition of IPTG to a final concentration of 0.1 mM and allowed to grow overnight at 20 ºC. Cells were harvested by centrifugation and disrupted with a French pressure cell press in 50 mM sodium phosphate buffer, pH 8.0, with 0.5 mg/mL lysozyme, 5 mg/mL DNase, 7 mg/mL pepstatin, 1 mM PMSF and 10 mg/mL leupeptin. The soluble fraction was clarified and applied over a Ni-NTA column. The VP6 protein then was eluted with the above buffer with 400 mM imidazole. The eluate was concentrated in Amicon Ultra filter

tubes (Millipore) and resolved on a Superdex 200 10/300 GL column (GE Healthcare) calibrated with reference proteins of 440, 158, 75 and 44 kDa molecular weights according to the manufacturer's instructions. This served as an additional purification step.

Expression and purification of RV6-26 Fab. RV6-26 heavy and light chain variable region genes were sequence-optimized and synthesized as cDNAs (GeneArt, Regensburg, Germany) based on antibody gene sequences that have already been published by our laboratory (GenBank, accession numbers AF452996 and AF453156, respectively). These synthetic genes were cloned into the pEE6.4 expression vector (Lonza) in-frame with a mouse kappa chain leader sequence at the 5′ end and optimized C_L and C_H1 constant domain sequences at the 3′ end, to encode a fully human Fab antibody fragment without affinity tags. The separate plasmids encoding heavy or light chain genes each were transformed into DH5α strain *E. coli* cells for large-scale plasmid DNA preparation (PureYield; Promega). Heavy- and light-chain encoding plasmid DNAs were co-transfected transiently into a high-producing clonal variant of the HEK-293 cell line cells (FreeStyle™ 293-F cells; Invitrogen) using Polyfect reagent (Qiagen), and the cells were incubated in humidified air with CO_2 in shaker flasks for 7 days. The supernatant was collected on day 7 and purified by fast protein liquid chromatography using an ÄKTA FPLC™ device and HiTrap KappaSelect column (GE Healthcare) in D-PBS, and then concentrated with 30 mL Amicon Ultra centrifugal filter units with 30 kDa molecular weight cut-off (Millipore). Crystallization requires a significant amount of protein. For higher expression of RV6-26 Fabs, the heavy and light chain variable region

cDNAs were cloned (using *Sal*I/*Not*I for light chain and *Eco*RI/*Hin*dIII for heavy chain) into pYD plasmid vectors optimized for high-level protein expression in 293-6E cells and containing C_K and C_H1, for heavy and light chains, respectively (15).

Crystallization. VP6 head domain crystals were grown by vapor diffusion of 13.9 mg/mL protein against a reservoir of 10% PEG 8000, 0.1 M sodium citrate pH 7.0 and 0.1 M Tris buffer pH 8.5. Crystals were cryoprotected by brief soaks in mother liquor supplemented with 20% glycerol and cooled in liquid nitrogen. RV6-26 Fab crystals were grown by vapor diffusion of 20 mg/mL protein against a reservoir of 2.0 M ammonium sulfate and 5% vol/vol 2-propanol. Crystals were cryoprotected by brief soaks in mother liquor supplemented with 20% glycerol and cooled in liquid nitrogen.

Data collection and structure determination. Diffraction data were collected from single crystals at 100K at sector LS-CAT 21-ID-G at the Advance Photon Source (Argonne, IL). Data were indexed, integrated and scaled with HKL2000 (47). Data collection statistics are given in Table 2-1. 5% of the data were randomly selected as an R_{free} set (8). Molecular replacement was performed with Molrep (69). The asymmetric unit contains a VP6 trimer, and all molecules were readily found by molecular replacement. Side chains that differed between the search model (bovine VP6) and the human VP6 were truncated to alanine and model was refined in Phenix (2). Refinement included rigid body refinement of the individual domains, simulated annealing, positional, individual B-factor, and TLS. Loops were rebuilt and side chains added in COOT (16) using simulated annealing composite omit maps (9) generated by Phenix (2). Non-

crystallographic restraints were imposed throughout refinement. TLS refinement (48) was incorporated in the final rounds of refinement using TLS groups identified using Phenix (2). The refined model consists three chains: chain A contains 151-337; chain B contains 156-331; chain C contains 156-331. In addition, the final model contains 492 water molecules. The final R_{factor} is 15.6%, the R_{free} is 17.1% for data between 50 and 1.7 Å. Additional data and model statistics are given in Table 2-1.

Diffraction data for RV6-26 Fab were collected from single crystals at 100K at sector LS-CAT 21-ID-D at the Advance Photon Source (Argonne, IL). Data were indexed, integrated and scaled with XDS, xdia2, and Scala (19, 25, 26, 59, 74). Data collection statistics are given in Table 2-1. 5% of the data were selected randomly as an R_{free} set (8). Molecular replacement was performed with Molrep (69) by iteratively searching a library of ~250 Fab fragments. The asymmetric unit contains two Fabs, and both molecules were readily found by molecular replacement. The best solution, obtained with Fab fragment from PDB-ID 1FDL, was identified based on the Contrast score. Side chains of this oriented model that differed from the 626 sequence were trimmed to alanine, and the resulting oriented model was refined in Phenix (2). Refinement included rigid body refinement of the individual domains, simulated annealing, positional, individual B-factor, and TLS. Loops were rebuilt and side chains added in COOT (16) using simulated annealing composite omit maps (9) generated by Phenix (2). Non-crystallographic restraints were imposed throughout refinement. TLS refinement (48) was incorporated in the final rounds of refinement using TLS groups identified using Phenix. The refined model consists two molecules, molecule A contains light chain amino acids 1-212 and heavy chain amino acids 1-220 molecule be contains light chain residues 2-

211 and heavy chain residues 1-221. In addition, two bound sulfates and 335 waters were included in the final structure. The final R_{factor} was 20.07%, the R_{free} is 23.50 for data between 50 and 2.6 Å. Additional data and model statistics are given in Table 2-1. The structure has been deposited in the Protein Data Bank under accession code 4HFW.

Hydrogen-deuterium exchange mass spectrometry. These studies were performed in collaboration with Virgil Wood's laboratory at University of California, San Diego. We performed comparative DXMS studies with a VP6hd construct alone or with VP6hd in complex with RV6-26 Fab. Prior to the deuteration studies, quench conditions optimal for maximum peptide fragmentation were determined, as previously described (24, 37). Complexes of VP6hd and Fab were prepared by mixing VP6hd and RV6-26 Fab at 1:1.4 stoichiometric ratio, and incubating the mixture at 0 °C for 30 minutes. The concept was to use an excess amount of Fab in the binding experiment to saturate all of the binding sites on VP6, and then to compare the hydrogen-deuterium exchange profile difference between VP6 alone and VP6-Fab complex. In similar experiments for paratope mapping on the RV6-26 Fab, we used an excess amount of VP6 to form complexes to ensure that all binding sites on Fab were occupied by VP6, and then compared the results between Fab alone and VP6-Fab complex.

Functional hydrogen-deuterium exchange reaction of free VP6hd was initiated by diluting 0.7 μL of stock solution into 1.3 μL of H_2O buffer (8.3 mM Tris, 150 mM NaCl, in H_2O, pH 7.15), and then mixed with 6 μL of D_2O buffer (8.3 mM Tris, 150 mM NaCl, in D_2O, pD_{READ} 7.15). At 10 sec, 100 sec or 1,000 sec, 12 μL of optimized quench reagent (0.8M GuHCl in 0.8% formic acid) was added to the respective samples and then

samples were frozen at -80 °C. The functionally-deuterated antibody-bound VP6hd samples were prepared by diluting 1.5 μL of complex solution (10.4 mg/mL for VP6 - RV6-26) into 0.5 μL of non-deuterated buffer, and then mixed with 6 μL of D_2O buffer (8.3 mM Tris, 150 mM NaCl, in D_2O, pD_{READ} 7.15). At 10 sec, 100 sec or 1,000 sec, 12 μL of optimized quench reagent was added to the respective samples and then samples were frozen at -80 °C. In addition, non-deuterated samples (incubated in H_2O buffer mentioned above) and equilibrium-deuterated back-exchange control samples (incubated in D_2O buffer containing 0.5% formic acid overnight at 25 °C) were prepared as previously described (24, 37, 40). Later, the samples were thawed automatically on ice and then immediately passed over an AL-20-pepsin column (16 μL bed volume, 30 mg/mL porcine pepsin (Sigma)), which was run at a flow rate of 20 μL/min with 0.05% trifluoroacetic acid. The resulting peptides were collected on a C18 trap and separated using a C18 reversed phase column (Vydac) running a linear gradient of 0.046% (v/v) trifluoroacetic acid, 6.4% (v/v) acetonitrile to 0.03% (v/v) trifluoroacetic acid, 38.4% (v/v) acetonitrile over 30 min with column effluent directed into an LCQ mass spectrometer (Thermo-Finnigan LCQ Classic) for epitope mapping or into an Orbitrap Elite mass spectrometer for paratope mapping. Data were acquired in both data-dependent MS:MS mode and MS1 profile mode. SEQUEST software (Thermo Finnigan Inc.) was used to identify the sequence of the peptide ions. The centroids of the isotopic envelopes of non-deuterated, functionally-deuterated, or fully-deuterated peptides were measured using DXMS Explorer (Sierra Analytics Inc., Modesto, CA), and then converted to corresponding deuteration levels with corrections for back-exchange (80).

Results

RV VP6 head domain expressed as a soluble protein that was recognized by an anti-RV antibody. I first determined if a VP6hd construct would express as a soluble protein. The VP6hd construct plasmid was expressed in bacteria, harvested, and purified using a Ni-NTA column. Figure 2-1 A shows the purified fraction of the expressed VP6hd resolved by SDS-PAGE and stained with Coomassie. The purified soluble fraction produced a band of about 25 kDa in size. I next sought to determine if a commercial polyclonal anti-RV-VP6 antibody could detect VP6hd. Figure 2-1 B shows a western blot of the 25 kDa VP6hd detected by a polyclonal anti-RV-VP6 antibody that also recognized the full-length VP6 protein. The recognition by the anti-VP6 antibody suggested that the VP6hd construct was properly folded.

RV VP6 head domain forms a trimer and binds to RV6-26 Fab. I next sought to confirm that the VP6hd construct forms a trimer and that it can still bind to RV6-26 Fab. Purified VP6hd, RV6-26 Fab and mixture of VP6hd:RV6-26 Fab in a 1:5 molar ratio of excess Fab, was resolved on a Superdex 200 10/300 GL column (GE Healthcare) calibrated with reference proteins of 440, 158, 75 and 44 kDa molecular weight according to the manufacturer's instructions. Figure 2-2 shows single peaks of RV6-26 Fab alone eluting at 50 kDa and VP6hd eluting at 75 kDa, when compared to the reference proteins. A distinct peak corresponding to a higher molecular weight of the VP6hd-RV6-26 Fab complex mixture was observed.

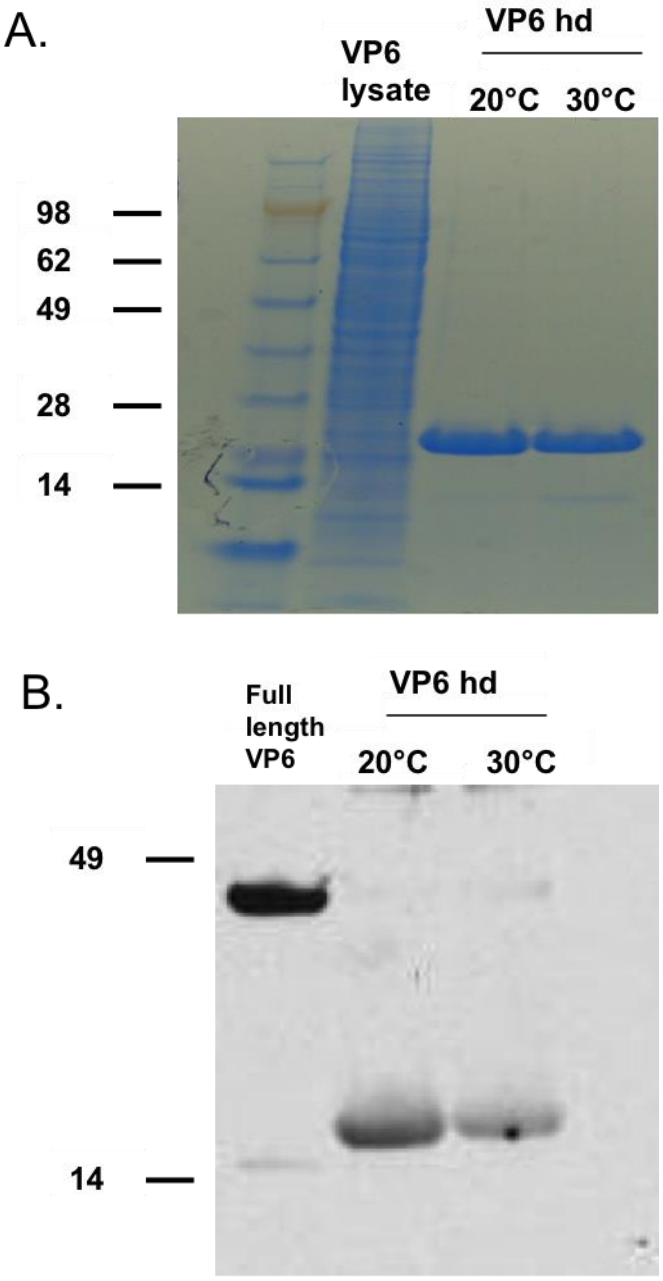

Figure 2-1. RV-VP6 head domain construct expresses as a soluble protein and can be detected by anti-RV antibodies. Panel A shows a Coomassie stained SDS-PAGE of bacterially expressed VP6hd. The purified soluble fraction shows a 25 kDa band of protein that expresses at both 20 ^{o}C and 30 ^{o}C. Panel B shows a western blot of the purified protein fractions detected by a polyclonal anti-RV antibody. Full length VP6 and the expressed VP6hd were both detected by the antibody.

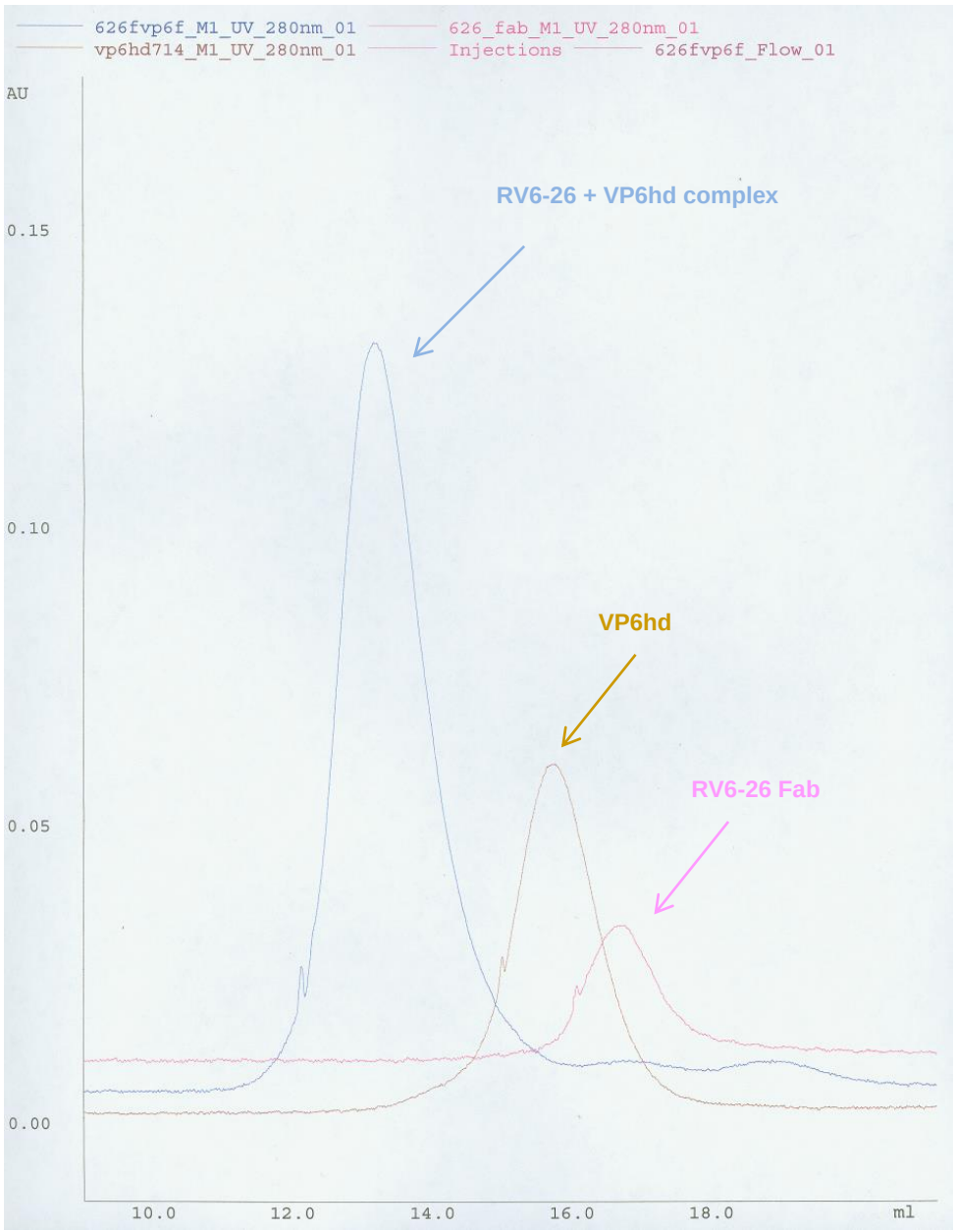

Figure 2-2: VP6hd forms a trimer and can bind to RV6-26 Fab to form a stable complex. Purified VP6hd and RV6-26 Fab proteins eluted as single peaks (pink and gold traces, respectively) from a Sephadex 200 column. A 1:5 molar ratio mixture of VP6hd:RV6-26 Fab resulted in a distinct shifted peak (blue trace) corresponding to the formation of a larger molecular weight complex of VP6hd:RV6-26 Fab. A slight bump on the blue trace can be observed underneath the RV6-26 Fab alone peak indicating the elution of excess Fabs from the complex.

X-ray crystal structure of VP6 head domain and RV6-26 Fab. After establishing that we have successfully designed and expressed the VP6hd construct, we proceeded to determine the x-ray crystal structure of VP6hd. We crystallized the VP6hd construct by hanging drop vapor diffusion in a buffer containing 10% PEG 8000, 0.1 M sodium citrate pH 7.0 and 0.1 M Tris buffer pH 8.5 (Figure 2-3 A) and the RV6-26 Fab also by hanging drop vapor diffusion in a 2.0 M ammonium sulfate and 5% vol/vol 2-propanol buffer (Figure 2-3 B). Diffraction data collection and refinement statistics for both structures are given in Table 2-1.

The VP6hd crystals (Figure 2-3 A) diffracted to a resolution of 1.7 Å revealing an expected trimeric structure comprised mainly of a jelly-roll β-barrel (Figure 2-4 A) as observed in the published structure of the full length VP6 protein (42). Two antiparallel β sheets, one with four β strands (labeled CHEF) and the other with six β strands (labeled A′A″BIDG) form the core of the jelly roll motif with a β hairpin insertion (D′D″) into the motif. The D′D″ β hairpin runs almost perpendicular to the A′A″BIDG β sheet and coordinates the majority of the packing contacts with the adjacent VP6 protomer. The CHEF β sheet lies on the outer surface, while the A′A″BIDG β sheet lies at the center of the domain (Figure 2-4 A). The top of the VP6 head domain is composed of loops βA′-βA″, βB-βC, and βH-βI, which includes a short αA helix (Figure 2-4 B). Structural comparison of the VP6hd structure to the published full length VP6 (PDB 1QHD) (42) by Chimera software yielded a RMSD of 0.635 (Figure 2-5).

The RV6-26 Fab crystals (Figure 2-3 B) diffracted to a resolution of 2.6 Å. The Fab assumes the typical immunoglobulin fold consisting of a heavy and a light chain,

A.

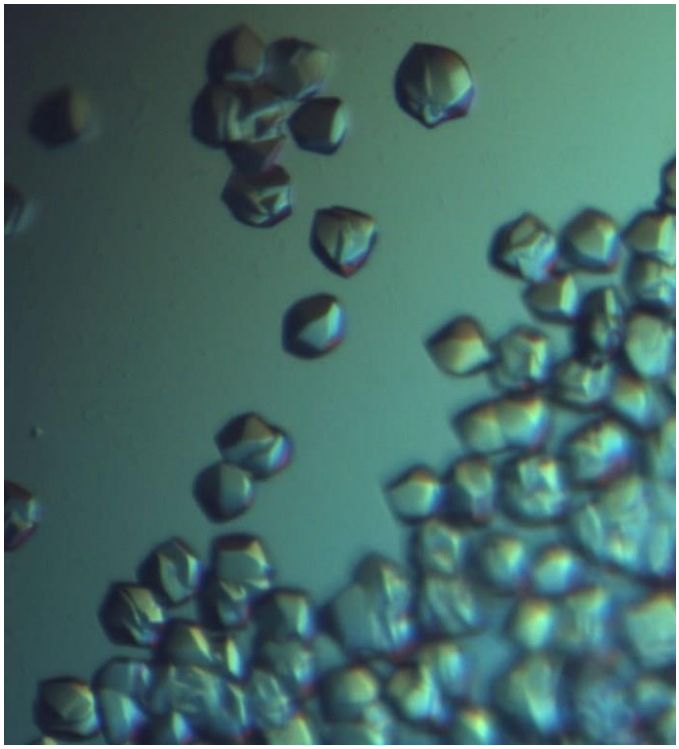

B.

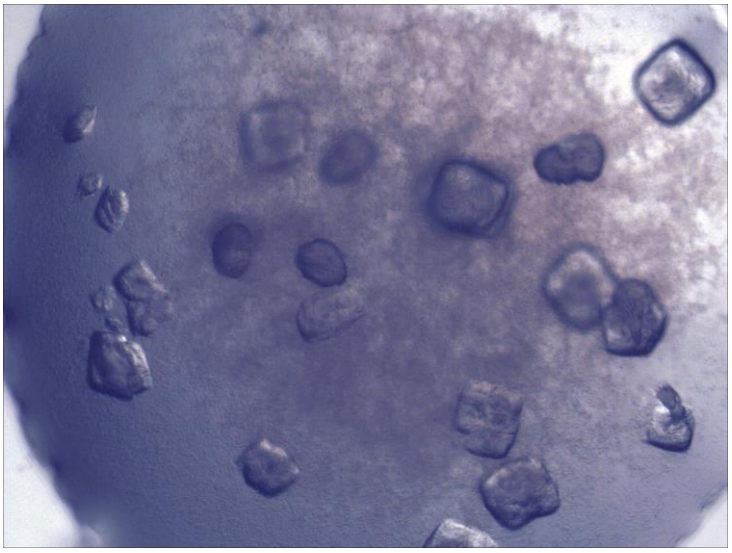

Figure 2-3: Crystals of VP6 head domain and RV6-26 Fab. (A). Crystals of VP6hd were grown by hanging drop vapor diffusion in 10% PEG 8000, 0.1 M sodium citrate pH 7.0 and 0.1 M Tris buffer pH 8.5. (B) Crystals of RV6-26 Fab were grown by hanging drop vapor diffusion in 2.0 M ammonium sulfate and 5% vol/vol 2-propanol.

Table 2-1. Data collection and refinement statistics

	VP6 head domain	RV6-26 Fab
Data collection		
Space group	$P3_121$	$P2_1$
Cell parameters	a=b=86.72	a=68.10
	c=163.8	b=97.92
		c=94.23
		□=108.9
Wavelength	0.97850	0.97850
Resolution (Å)	50-1.7	50-2.6
Completeness (%)	50-1.7 Å: 100 (99.7)	50-2.25 Å: 99.7 (100)
Redundancy	50-1.7 Å: 7.5(4.8)	50-2.6 Å: 4.2(4.2)
I/sigmaI	50-1.7 Å: 24.0 (2.7)	50-2.6 Å: 8.5(2.2)
Refinement		
Resolution (Å)	50-1.7 Å	50-2.6 Å
No. reflections	78,480	35,513
Working set		
No. reflections free set	3,940	1,778
R_{work} / R_{free} %	15.6/17.1	20.07/23.50
R.m.s. deviations		
Bond lengths (Å)	0.005	0.004
Bond angles (°)	1.084	1.108
Ramachandran Plot	Favored=98.3%	Favored=98.1%
	Allowed=1.68%	Allowed=1.65%
	Outliers=0 %	Outliers=0.24%

A.

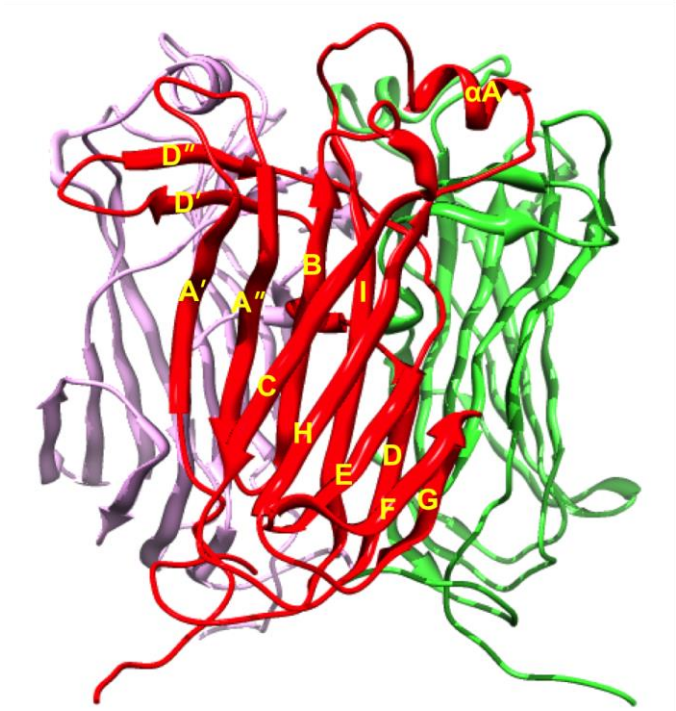

B.

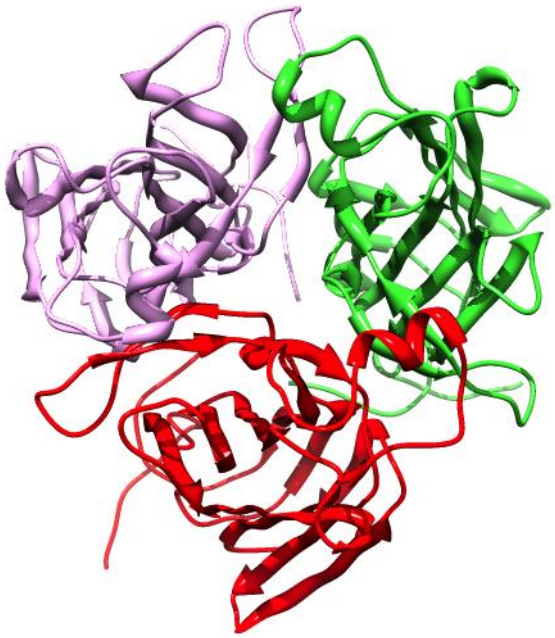

Figure 2-4: Ribbon diagram of VP6 head domain. (A). Ribbon diagram of VP6hd trimer showing the three protomers colored in red, green and purple. The jelly-roll is labeled according to standard nomenclature for jelly-roll motifs (58). (B). Top view of the VP6hd structure showing the loops and short α-helices on top of the VP6 structure. Ribbon representation was made using Pymol software (60).

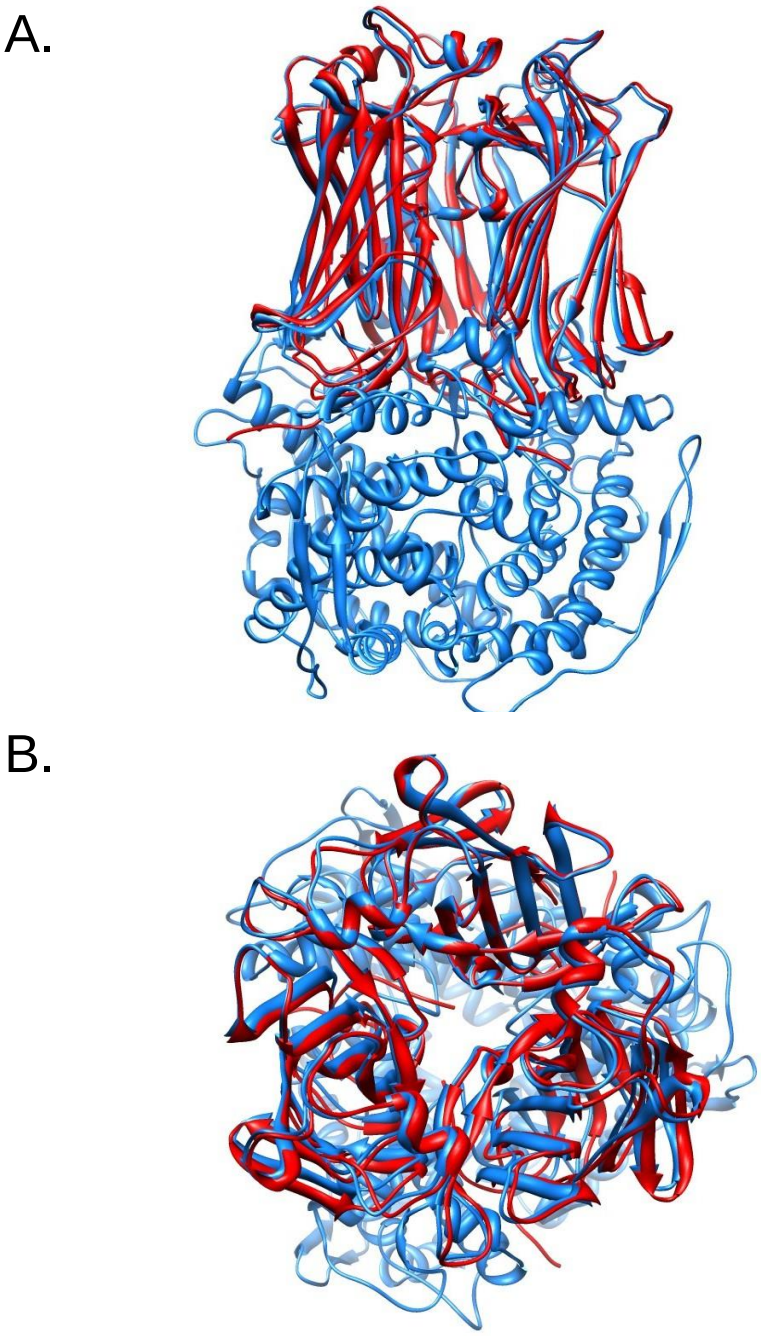

Figure 2-5: Ribbon diagram of VP6 head domain in comparison to the full length VP6. Side view (A) and top view (B) of the ribbon diagram of VP6hd trimer (red) superimposed on the full length VP6 trimer (blue) [PDB 1QHD]. Superimposition was performed using Chimera software (49).

each containing a constant domain (C_H1 and C_L for the heavy and light chains, respectively) and a variable domain (V_H and V_L) Six complementarity-determining regions (CDRs), three from each variable domain form the antigen-binding site. Figure 2-6 shows ribbon diagram of the molecular structure of the Fab. The quaternary structure of RV6-26 Fab is that of an extended conformation, with the variable and constant domains well separated. The extended conformation is also usually described by reference to an "elbow" angle made by the pseudo two-fold axes relating the two variable domains (V_H to V_L) and the two constant domains (C_H1 to C_L).

RV6-26 binds to a quaternary epitope of VP6 encompassing two different regions on adjacent protomers. In collaboration with Virgil Woods' laboratory at the University of California, San Diego, we next sought to determine the contact surface of RV6-26 to VP6 using enhanced amide hydrogen/deuterium exchange mass spectroscopy (DXMS). The principle of DXMS analysis is that amide hydrogens on the surface residues of proteins exchange readily with deuterated hydrogen in the protein buffer. When antibody binds and the surface residue is now buried, the amide hydrogens can no longer be exchanged because the surface residues are now buried and inaccessible, thus suggesting the residues comprising the epitope. Using DXMS, we identified the epitope of RV6-26 on VP6, which involved peptides derived from regions including residues 231 – 260 and 265 – 292 (Figure 2-7 A). When we labeled those residues on a space-filling model of the structure of the VP6 trimer, it became apparent that there were two separate regions (which we designated region A [amino acids 231-260] or B [amino acids

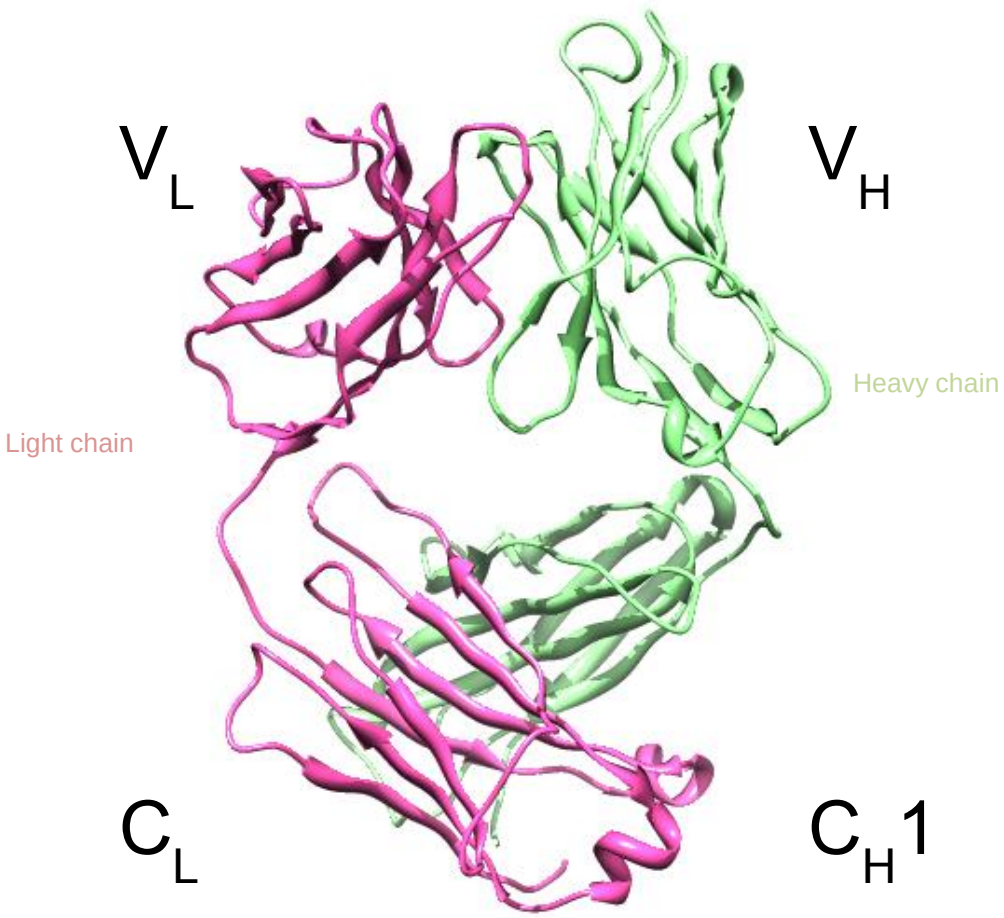

Figure 2-6: Ribbon representation of the topology of RV6-26 Fab as determined at 2.6 Å. The light chain is in pink and the heavy chain is in green. The variable domains containing the antigen-binding loops are in the upper portion of the structure, while the constant regions are below. The figure was produced using Pymol software (60).

265-292]) on each VP6 protomer that were recognized by the Fab. Region A spanned from the loop emanating from βD through the D′D″ β-hairpin, inserted into the jelly-roll motif of the VP6 head domain, and ended at the base of βE, with the D′D″ hairpin. The hairpin also was responsible for most of the interactions between head domains at the top of the trimer (42). Region B extended from the tip of βE through strands F, G and H of the jelly-roll β-barrel. This epitope region is within the CHEF β-sheet that lies on the exposed side of VP6. When we examined the arrangement of the epitope regions A and B from each protomer in the configuration of VP6 trimers on the DLPs, it is clear that the Fab could only bind to regions A and B when they formed a continuous epitope at the junction of two protomers (Figure 2-7 B-C); an Fab could not bind to region A and B on a single protomer. Thus, RV6-26 recognizes a quaternary epitope that is formed as continuous surface using regions from two protomers of the same trimer.

Discussion

Our laboratory has previously isolated RV6-26, a member of the immunodominant gene segment in response to rotavirus infection, and performed extensive biochemical studies to characterize its interactions with RV-VP6 (27, 70-73). However, the specific residues that were involved in the antigen-antibody interaction remained unresolved. The most direct way to determine the exact residues involved in the binding interface is by determining the crystal structure of the bound Fab-VP6 complex. Previous structural modeling studies in our laboratory have identified the head domain of the VP6 protein as the most likely location of the RV6-26 epitope (44). Furthermore, in the context of the RV-DLP structure, the VP6 base domain is buried in deep in the VP6

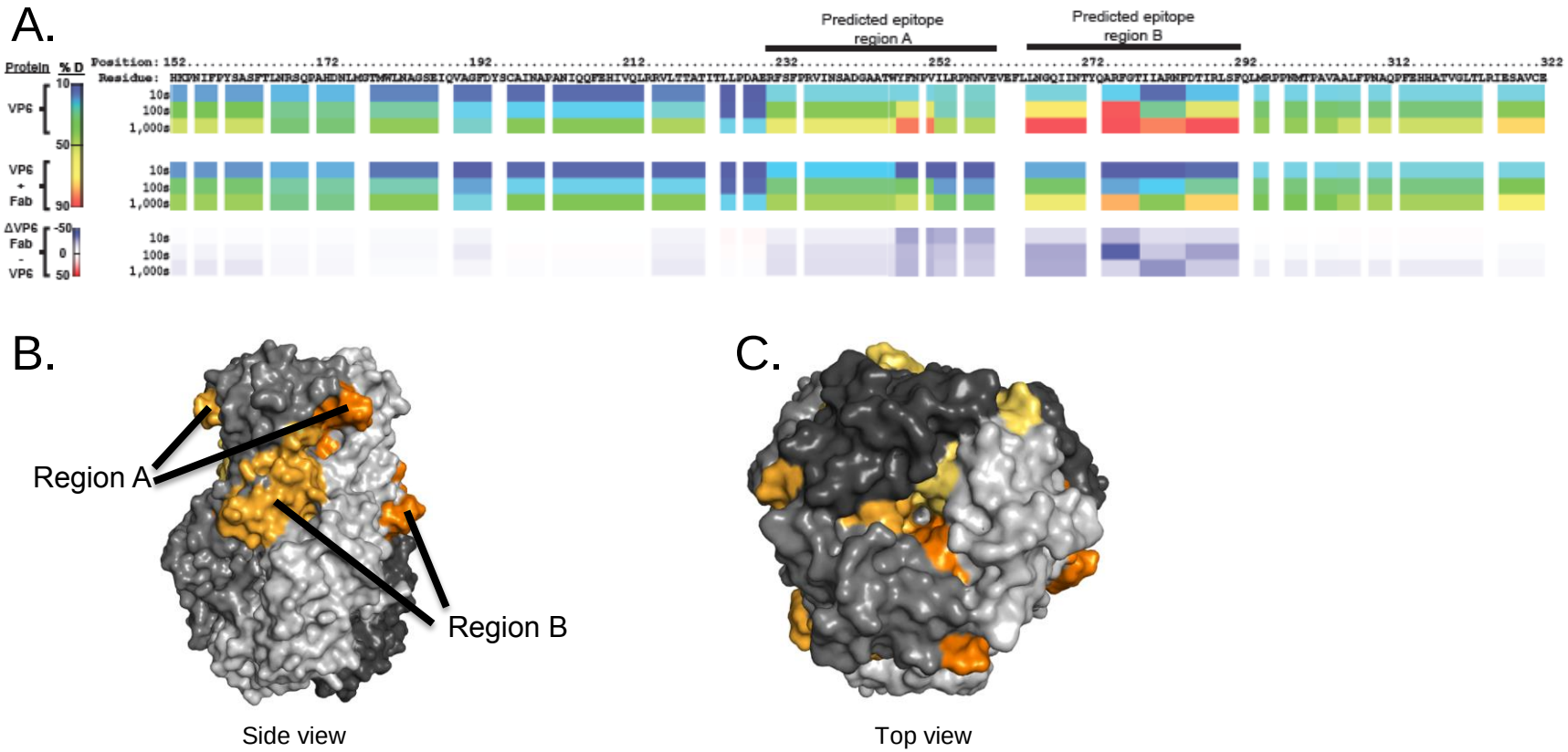

Figure 2-7: Determination of VP6 epitope for RV6-26 by hydrogen-deuterium exchange mass spectroscopy. Ribbon map showing percent deuterated (%D) of VP6hd alone (top band), or VP6hd bound to RV6-26 Fab (middle band). The top row shows the residue position number, the second row shows the residue and the rest of the rows show protein dynamic features at different on-exchange timepoints (10, 100 or 1,000 seconds [s]). As indicated in the colored bar, cold colors suggest relatively stable regions and warm colors suggest relatively flexible regions. All prolines are shown in white because prolines do not have amide hydrogens. Residues uncovered by surface deuteration are also shown in white. Difference map showing the influence of RV6-26 Fab binding to VP6 indicated by changes in % D (bottom band). Blue suggests the regions that exchange slower upon Fab binding; red suggests the regions that exchange faster upon Fab binding. (B) Side view of the predicted epitope regions of RV6-26 Fab on the VP6 structure (PDB: 1QHD). The different shades of gray represent the three protomers that make up the VP6 trimer, and the different shades of orange represent the predicted epitope regions A and B mapped on each protomer. Region A on one protomer and region B on a different protomer are visible. (C) The top view of the VP6 trimer with all the predicted epitope regions visible on the structure.

layer and mainly interacting with the inner VP2 layer (43) and thus will be inaccessible to the antibody. These reasons, together with the relative ease of crystallizing a smaller protein, provided the rationale for designing the VP6hd construct.

Our attempts to determine the x-ray crystal structure of RV6-26-VP6 complex have so far been unsuccessful. Nevertheless, we successfully determined the structures of the VP6hd and RV6-26 Fab as separate individual molecules. We used the reagents and data generated from the crystallography studies to employ an alternate biochemical technique, DXMS, to determine the epitope of the RV6-26. The DXMS studies revealed a quaternary epitope recognized by RV6-26. This result indicating the quaternary nature of epitopes recognized by inhibitory human Fabs is consistent with some previous epitope mapping studies of murine inhibitory Fabs. The main difference observed between the inhibiting and non-inhibiting Fab was in the location of their epitopes (66). The epitope of inhibitory Fabs involved multiple loops on two VP6 protomers, while only one VP6 protomer was involved in binding of the non-inhibitory Fabs. That the RV6-26 epitope is of a quaternary nature may explain it inhibitory function.

Chapter summary

In this chapter, I present data that demonstrate a viable and stable VP6 head domain construct is feasible. Second, I show that this construct can successfully be crystallized and the structure determined by x-ray crystallography. Finally, I show that an alternate technique such as DXMS, can be used to deduce the epitope of an antibody. DXMS revealed a quaternary epitope for RV6-26 could explain its inhibitory function.

CHAPTER III

MECHANISM OF ANTI-VIRAL ACTIVITY OF RV6-26 FAB

Introduction

Rotavirus, in its TLP form, is transcriptionally-inactive; the DLP is transcriptionally-active (4, 12, 56, 78). The viral transcription machinery, composed of VP1 and VP3, is located near the icosahedral five-fold axis below the VP2 layer (53). In the TLP, VP7 obstructs the Type I channels located at the five-fold axes, causing a steric hindrance that blocks the exit of nascent mRNAs (36). Recent structural studies have shown that VP7 also induces a global conformational change in the VP6 trimer arrangement that results in a narrowing of the Type I channels at the five-fold axes as observed in the high-resolution cryo-EM structure of the DLP recoated with recombinant VP7 [13]. The fact that VP7 changes the orientation of the VP6 timers around the Type I channel also was noted in an earlier moderate resolution cryo-EM study comparing VP2–VP6 with VP2–VP6–VP7 recombinant particles (21).

The epitope of RV6-26 Fab has been determined in the previous chapter. Given that RV6-26 has inhibitory function (27), we sought to understand the mechanism to antiviral activity of the antibody. To achieve this goal, we employed the use of cryo-EM analysis, together with computational modeling aided by biochemical data from DXMS, to determine the binding mode, and hence the mechanism of inhibition of the antibody.

Materials and methods

Preparation and purification of rotavirus double-layered virus particles (DLPs). A strain of rhesus rotavirus (RRV) was kindly provided by Susana López (Universidad Nacional Autónoma de México). Virus was inoculated onto cell culture monolayers of MA-104 cells (CRL-2378.1; ATCC, Manassas, VA) at low MOI. When cell monolayers exhibited significant cytopathic effect, the supernatant and cell fractions were collected and virus was isolated by ultracentrifugation in a Sorvall Discovery 90SE centrifuge with a Surespin 630 rotor at 20,000 rpm for 1.5 hours at 4 °C. The resulting pellet was resuspended in Earle's Balanced Salt Solution (GIBCO®) and the cellular debris was removed by addition of 1,1,2-trichloro-trifluoroethane (EMD Chemicals) and blending. The suspension then was centrifuged at 2,000 rpm for 0.5 hours at 4 °C to separate virus from cell debris. Virus particles then were collected and purified by ultracentrifugation through a CsCl cushion at 20,000 rpm for 1.5 hours. To prepare concentrated DLPs, the collected viral particles were treated with 10 mM EGTA (Lonza) for 5 minutes at room temperature to remove the outer VP4 and VP7 protein layers of the rotavirus triple-layered particles. The resulting DLPs were purified further by CsCl density gradient ultracentrifugation at 29,700 rpm for 20 hours. The visible band containing DLPs was collected and concentrated further by ultracentrifugation in the same CsCl density gradient at 29,700 rpm for 2 hours. The band then was collected and dialyzed into Tris-buffered saline (Mediatech).

Cryo-electron microscopy. These studies were performed in collaboration with Phoebe Stewart's laboratory in the Department of Molecular Physiology and Biophysics. Purified

DLPs were mixed with five-fold molar excess of purified RV6-26 Fab protein, and then the excess antibody was removed using centrifugal filters with Sephadex G-50 resin. The complexes of RV DLPs with RV6-26 Fab in Tris-buffered saline pH 8.0 with 0.5% glycerol were applied to freshly prepared electron microscopy (EM) grids with a holey carbon film. The excess liquid from a 2-3 μL droplet was blotted away with filter paper. Another 2-3 μL droplet was added to the same EM grid and excess liquid was blotted as before. The sample grid was plunged immediately into liquid ethane cooled by liquid nitrogen. All data was collected on an FEI Tecnai Polara microscope equipped with a field emission gun (FEG) operating at 300 kV in nanoprobe mode. The sample grids were maintained at liquid nitrogen temperature during data acquisition. Images were recorded digitally on a Gatan UltraScan 4000 (4k x 4k) CCD camera. Micrographs were collected with a defocus range of 0.5 - 5 μm and with an absolute magnification of 199,000x.

Image processing and reconstruction. Individual particle images were centered manually, cropped and binned using in-house scripts (developed in Phoebe Stewart's laboratory) in conjunction with IMAGIC and EMAN image processing suites. A total of 3,029 particle images was picked and processed in this dataset. Images were binned and stacked with 6.0 and 3.0 Å pixel sizes. 6.0 Å stacks were used for initial CTF parameter determination using CTFFIND3. Orientation, magnification and defocus parameter determination and refinement were carried out using FREALIGN. Image processing was carried out through 34 rounds of FREALIGN refinement, converging at a resolution of 10.9 Å, at a pixel binning of 3.0 Å. Resolution was determined as measured by the Fourier shell correlation (FSC) 0.5 criterion. Icosahedral symmetry was imposed during data processing. Docking

of coordinates for a ring of five VP6 trimers extracted from the crystal structures of the rotavirus DLP (PDB-ID 3KZ4) and the infectious rotavirus particle (PDB-ID 3N09) was performed with the UCSF Chimera Fit-In-Map function. The same coordinate sets also docked into segments of the DLP cryo-EM structure (EM Data Bank EMD-1460), the VP7 recoated DLP cryo-EM structure (EM Data Bank EMD-1571), and the cryo-EM structure of the RV6-26-DLP complex. The voxel size of each cryo-EM density map was varied in Chimera by plus or minus a few percent to maximize the reported average map value. The resulting set of average map values were normalized and plotted for each cryo-EM structure.

Computational docking of Fab to VP6 epitope. These studies were conducted in collaboration with David Nannemann in Jens Meiler's laboratory in the Department of Chemistry. Prior to docking, VP6 trimer and RV6-26 were relaxed using the Rosetta FastRelax protocol with a harmonic restraint placed on all Cα pairs within 8 Å using a standard deviation of 0.5 Å. The VP6 trimer was submitted to five rounds of relax, while the antibody variable domain underwent rounds of relaxation until energy and geometry converged. The ten top-scoring VP6 and RV6-26 models were carried into docking, with each docking run performed with all pairwise combinations of antibody and antigen. To decrease the time required for generation of each model, docking was performed with a single VP6 trimer and only the variable domains of the antibody. We performed a conformational search during docking, allowing 3 Å translational and 8° rotational perturbations of the antibody relative to antigen during the low-resolution search and 0.1 Å translational and 3° rotational perturbations during the high-resolution search (12).

Several different approaches for incorporation of DXMS data were explored. First, interaction between surface residues within the inferred epitope and paratope was encouraged through addition of distance restraints to C-α atoms across the interface. Alternatively, non-overlapping segments of the epitope and paratope were determined from the DXMS data, and each segment formed the basis for a single restraint. In each case, the restraint was fulfilled if any amino acid C-α atom within a contiguous peptide segment had a Euclidean distance below 8 Å to a C-α atom of the partner protein. A flat harmonic penalty with a standard deviation of 2 Å was added to the score if no amino acid within the segment fulfilled the restraint. All Rosetta experiments were performed within the RosettaScripts framework (22) with Rosetta revision 49262. To simulate cryo-EM densities, a fully occupied channel was generated through alignment of the VP6:RV6-26 complex model to each trimer in a channel extracted from the crystal structure of the rotavirus DLP. Antibody constant domains were added back through alignment of the RV6-26 Fab crystal structure with the model. Cryo-EM densities of the fully saturated channel were simulated with BCL::PDBToDensity (33) at a resolution of 10.9 Å and voxel size of 3.02 $Å^3$ and Gaussian noise added to the simulated map for an overall CCC of 0.5 for the simulated map to the noised map. Cross-correlation coefficients of simulated and experimental antibody densities were calculated within Chimera after optimally aligning the VP6 channel.

Results

Generation and purification of RV-DLPs and RV6-26-DLP complexes. To obtain a high-resolution cryo-EM structure, it is important to use high-quality reagents including stable and homogenous DLPs of high integrity. Figure 3-1 A shows a transmission electron micrograph of a representative RV-DLP prep that is to be used to make Fab-DLP complexes. All the particles are uniform with distinct defined edges indicating that they were intact particles suitable for cryo-imaging. Further, we tested the effect of binding Fabs to the RV-DLPs to make sure that the Fab-DLP complexes that formed were also intact particles. Figure 3-1 B shows that the RV6-26 Fab and DLPs formed stable complexes suitable for cryo-imaging.

Image processing of RV6-26-DLP complex structure. After cryo-imaging of the prepared Fab-DLP complexes, full intact particles were hand picked from the cryo-micrographs as shown in Figure 3-2 A and processed into stacks shown in Figure 3-2 B using edited in-house scripts developed in Phoebe Stewart's lab.

3D reconstruction and cryo-EM structure of the RV6-26-DLP complex. I determined the pattern of binding of RV6-26 to DLP. To determine the specific mechanism of action, RNA transcription occurs at the base of the Type I channel, which is located at the icosahedral five-fold symmetry of the VP6 layer. The VP1 and VP3 transcription complex assembles on the VP2 core at each of the five-fold axes of the virion particle. We sought to determine if RV6-26 bound to DLPs at this channel, and if so, to define the mode of binding. We determined the structure of complexes of RV6-26 Fab and

A.

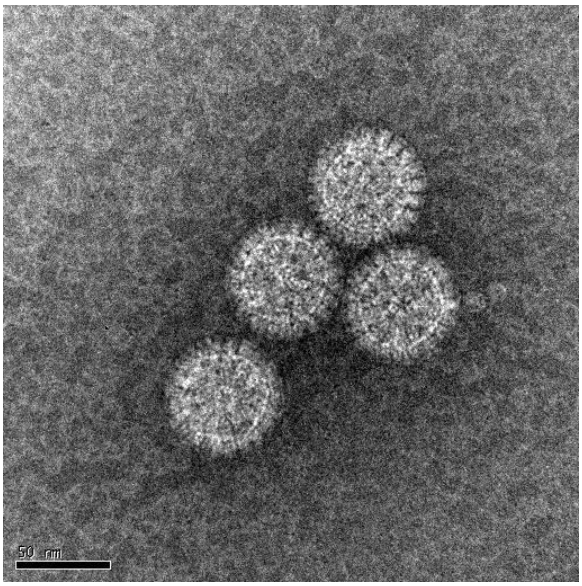

B.

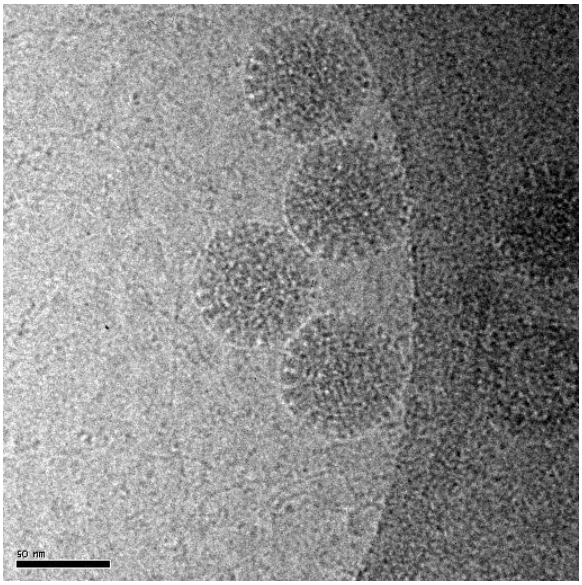

Figure 3-1. Micrographs of RV-DLPs and RV6-26-DLP complexes. (A). Representative image of purified DLPs, applied to a grid, stained with uranyl formate, and visualized by negative stain EM. (B). Representative image purified RV6-26-DLP complexes in ice. Images were collected on a 120 KeV Tecnai LaB_6 microscope. Scale bar, 50 nm.

A.

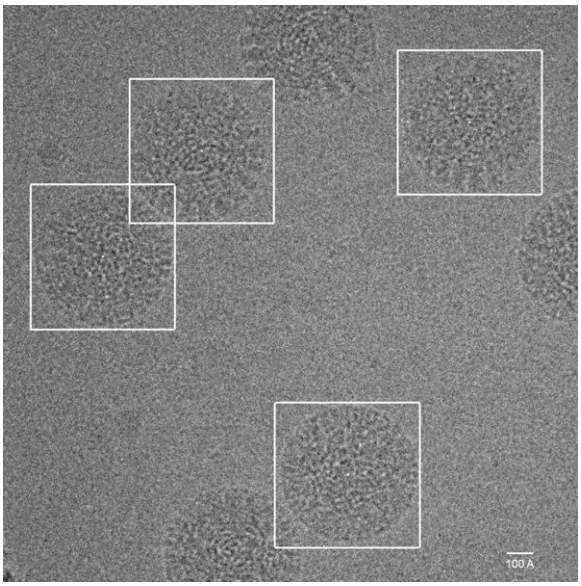

B.

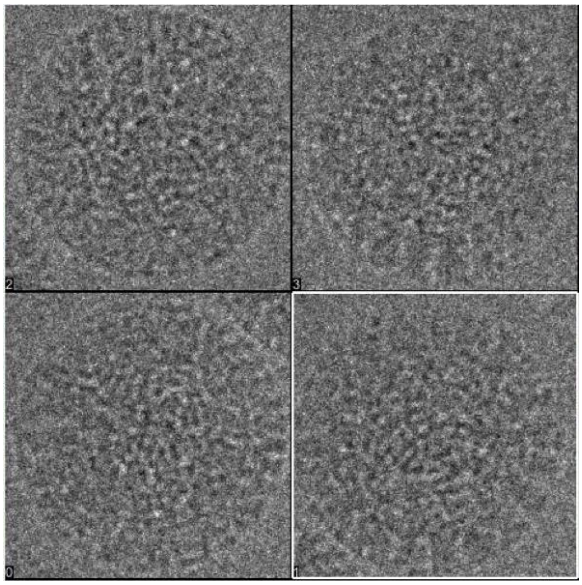

Figure 3-2. Cryo-micrographs of RV6-26-DLP complexes used in the 3D reconstruction of the RV6-26-DLP structure. (A). Representative image of purified DLPs in vitreous ice with complete intact particles used for further processing in white boxes (B). Representative image showing boxed image stacks resulting from picked particles that are further processed for 3D reconstruction. Images were collected on a FEI Tecnai Polara TF30 microscope. Scale bar, 100 nm.

RV DLPs using cryo-electron microscopy (cryo-EM) reconstruction. The reconstruction of the Fab-DLP complex was computed from 3,029 complex particle images extracted from corresponding cryo-EM micrographs as shown in Figure 3-2. Numerous cryo-EM structures have been determined for icosahedral viral particles in complex with antibodies and receptors (65). Normally, the antibody or receptor extends away from the viral surface and is visible in cryo-electron micrographs. Even Fab fragments bound to viral particles typically are visible in the cryo-electron micrographs (11, 51). In the case of the Fab-DLP complex, the cryo-electron micrographs revealed that the particles were smooth without any projecting Fab density (Figure 3-2 A). After image reconstruction the estimated final resolution for the Fab-DLP complex was 10.9 Å, using the 0.5 FSC criterion (Figure 3-3 B). Consistent with the cryo-electron micrographs, the structure also was relatively smooth on the surface with the Fab density situated between VP6 trimers rather than protruding from the outer surface of the viral particle (Figure 3-3 A).

RV6-26 exhibits asymmetric binding to the VP6 molecules in the Type I, II, and III channels on DLPs. The complex structure revealed a number of interesting features of binding. Type I, II, and III channels of the DLP clearly were occupied by the Fab. Interpretation of the data was complicated, as reconstructing the density map from 3,029 particles averaged the density of Fabs bound to these channels. For example, we observed Fab density only in the center of the channel, not directly touching the DLP. Further, the Fab density was much smaller than the expected size of a Fab - approximately only 14,

A.

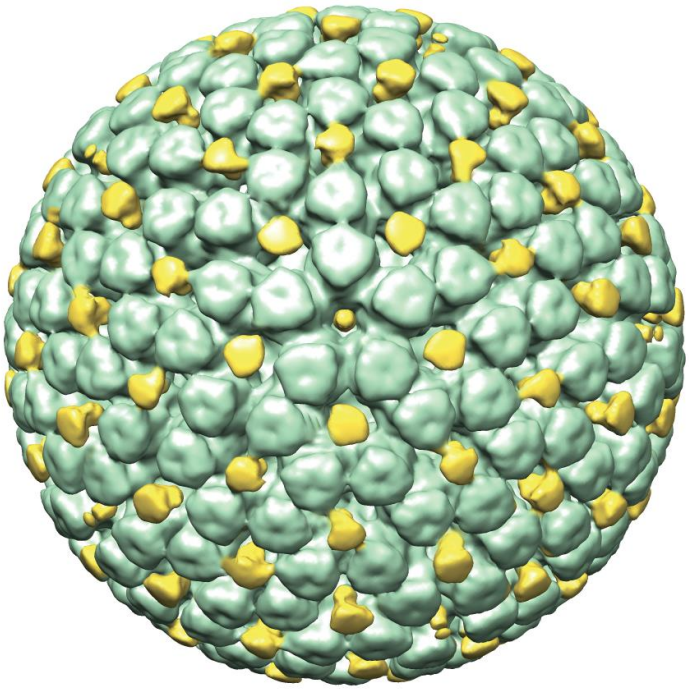

B.

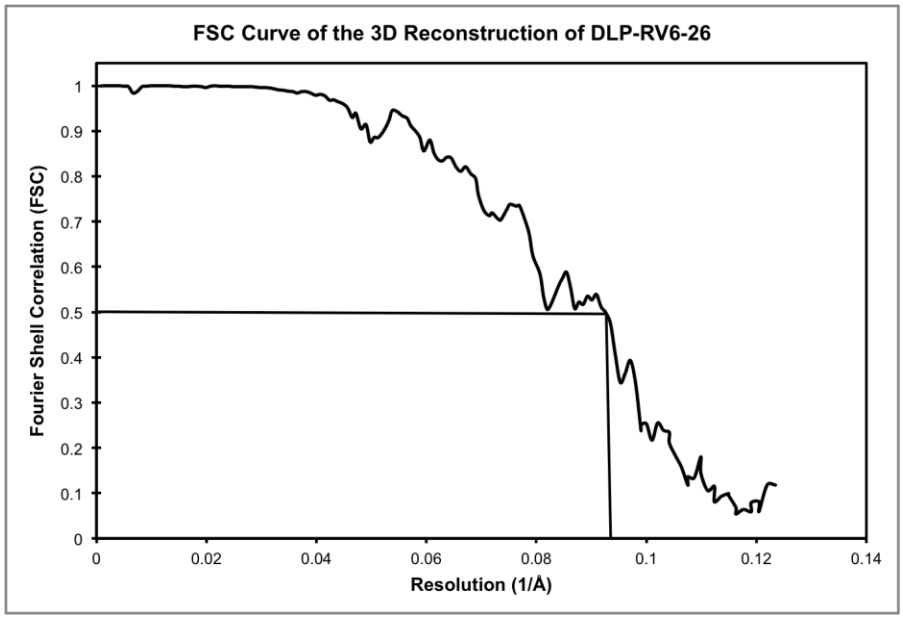

Figure 3-3: 3D reconstruction of the RV6-26-DLP complex to a resolution of 10.9 Å. (A). Surface representation of the structure of RV6-26-DLP complex with the outer VP6 layer in green and the RV6-26 Fabs in yellow. (B). FSC curve of the complex reconstruction showing FSC 0.5 resolution at 10.9 Å.

34 and 31% for channel Type I, II and III, respectively. We attribute this finding to the fact that only one Fab can fit into each channel at any given point in time. If one Fab is bound in each channel and this binding is not preferential toward any one VP6 trimer, then the contribution of the Fab would be averaged due to the imposed icosahedral symmetry in differing ways in the Type I, II or III channels. Density at the Fab-DLP interface is expected to be weakened to 20% (Type I channel) and 17% (Type II and Type III channels) and to be present at 100% only where Fabs binding to different trimers overlapped. For Type I channels a perfectly five-fold symmetric Fab density was observed, because the Type I channel is located at the five-fold axis (Figure 3-4 A), and icosahedral symmetry is imposed in data processing. Asymmetric Fab reconstructions were observed at the quasi-six-fold axis (the Type II and Type III channels; Figure 3-4 B, C). This asymmetry can be explained by the fact that these channels are not perfectly symmetric but locate on the pseudo six-fold axis. If the hexagonal channel is deformed in one dimension, Fabs will overlap more extensively, leading to additional density in these areas. Alternatively, preferential binding or differential accessibility could explain the asymmetry. In the Type III channels, additional density links the Fab to the trimers, which are adjacent to the five-fold trimers and icosahedral three-fold trimers, respectively (Figures 3-4 C). However, a model assuming equal probability for all Fab-trimer interactions suggests that no preferential binding or differential accessibility is needed to explain the experimental results. The observed reduction in density for Fab was consistent with a single Fab binding in a non-preferential manner per channel.

A.

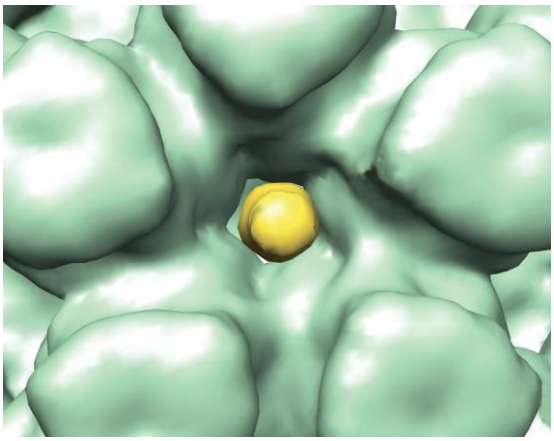

B.

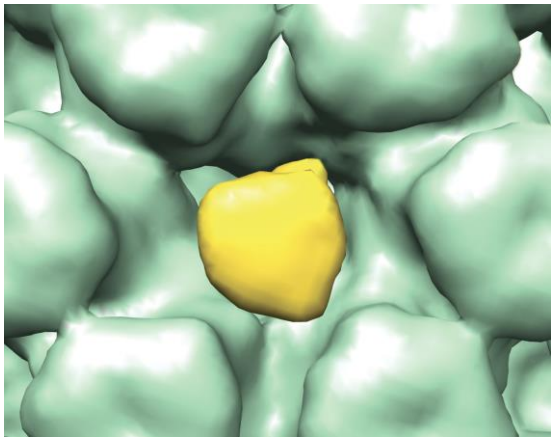

C.

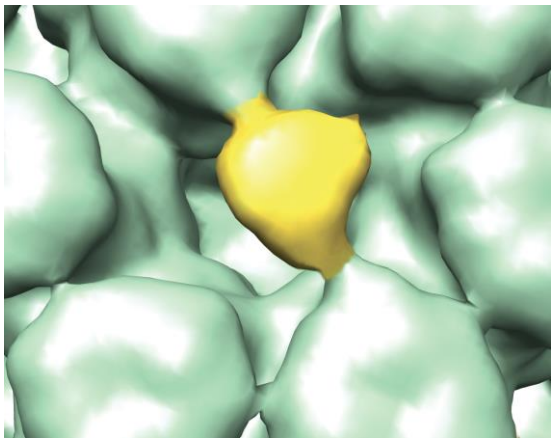

Figure 3-4: Binding pattern of RV6-26 Fab in the DLP Type I, II or III channels. (A). RV6-26 Fab (yellow) at Type I channel showing a diminished Fab density at the center of the five-fold axis. Asymmetric Fab reconstructions were observed at the Type II channel (B) and Type III channel (C) at the pseudo-six-fold axes.

Computational modeling of the RV6-26 Fab-VP6 interaction. In the previous chapter we used DXMS to determine the epitope of RV6-26. Concurrently, we also used DXMS as described in the previous chapter to determine the paratope (residues on the antibody that interact with VP6) of RV6-26 Fab. Residues 52-59, corresponding to the hypervariable complementarity-determining region 2 of the heavy chain (HCDR2) was shown to be strongly protected from exchange upon complex formation. In addition, residues 67-89 and 95-113 were implicated to be involved in the antigen-antibody interaction. The light chain residues 25-42 and 85-94 also were shown to be protected strongly upon complex formation. These residues were mapped onto the surface representation of the RV6-26 Fab (Figure 3-5).

We used computational docking with Rosetta to determine the fine specificity of the interaction. We docked atomic resolution structures of the RV6-26 Fab (PDB-ID 4HFW) and the VP6 trimer (PDB-ID 1QHD), both determined by crystallography, using the DXMS-determined epitope and paratope as restraints to guide the docking. Docking calculations were seeded from manually placed antibody locations that matched the DXMS and cryo-EM experimental data and from previously generated models (44). Trajectories with good predicted binding energies converged on a similar overall conformation of the RV6-26 variable domain region relative to the VP6 trimer, *i.e.*, a single low-energy binding mode consistent with the experimental DXMS data was identified. The interaction confirmed the quaternary nature of the epitope, with the antibody interacting with both region A and region B of adjacent VP6 protomers within a single VP6 trimer (Figure 3-6 A-B). Quaternary interaction was mediated largely by the heavy chain of RV6-26, which interacts with region A and region B, while the light chain

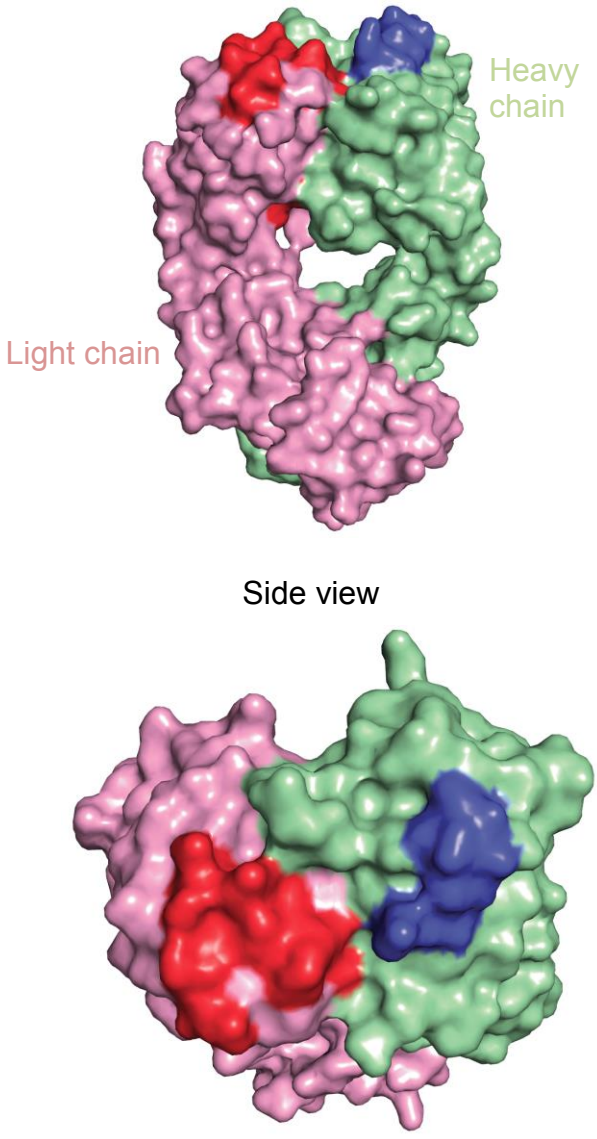

Figure 3-5: RV6-26 Fab paratope as determined by DXMS. Surface representation of RV6-26 Fab showing the light chain (pink) and heavy chain (green) with the paratope, as determined by DXMS, mapped onto the light and heavy chains in red and violet respectively.

predominantly interacted with region B. Significant contact was generated by HCDR2, in agreement with previous studies (27, 44). To test agreement with the cryo-EM reconstruction, we simulated densities of models from this binding mode assuming equal occupancy of each Fab-trimer interface in the Type I, II, and III channels (Figure 3-7 A-C). There are five epitopes at the Type I channel, but modeling indicates that steric hindrance between Fab fragments limits the number of Fab fragments bound per channel to a maximum of one. Similarly at the Type II and III channels, although there are six epitopes per channel there is only space for one Fab fragment to bind per channel. Significant correlation was observed between the models with the described conformation and the experimental density, with cross-correlation coefficients of 0.51, 0.72, or 0.77 for Type I, II, or III channels, respectively.

Correlation of simulated and experimental cryo-EM densities was highly dependent on even small changes (changes that did not alter the Fab-trimer orientation) in the interaction angle between the Fab and VP6 trimer. We selected the model with highest cross-correlation coefficient values for further analysis, and conclude that the cryo-EM and DXMS datasets are complementary, contributing different and important information to the model. We hypothesize that formation of the complex alters the elbow angle (22) of RV6-26 relative to the angle observed in the crystal structure of the Fab alone. These results corroborate the experimental findings, providing a general mechanism of interaction between RV6-26 and VP6.

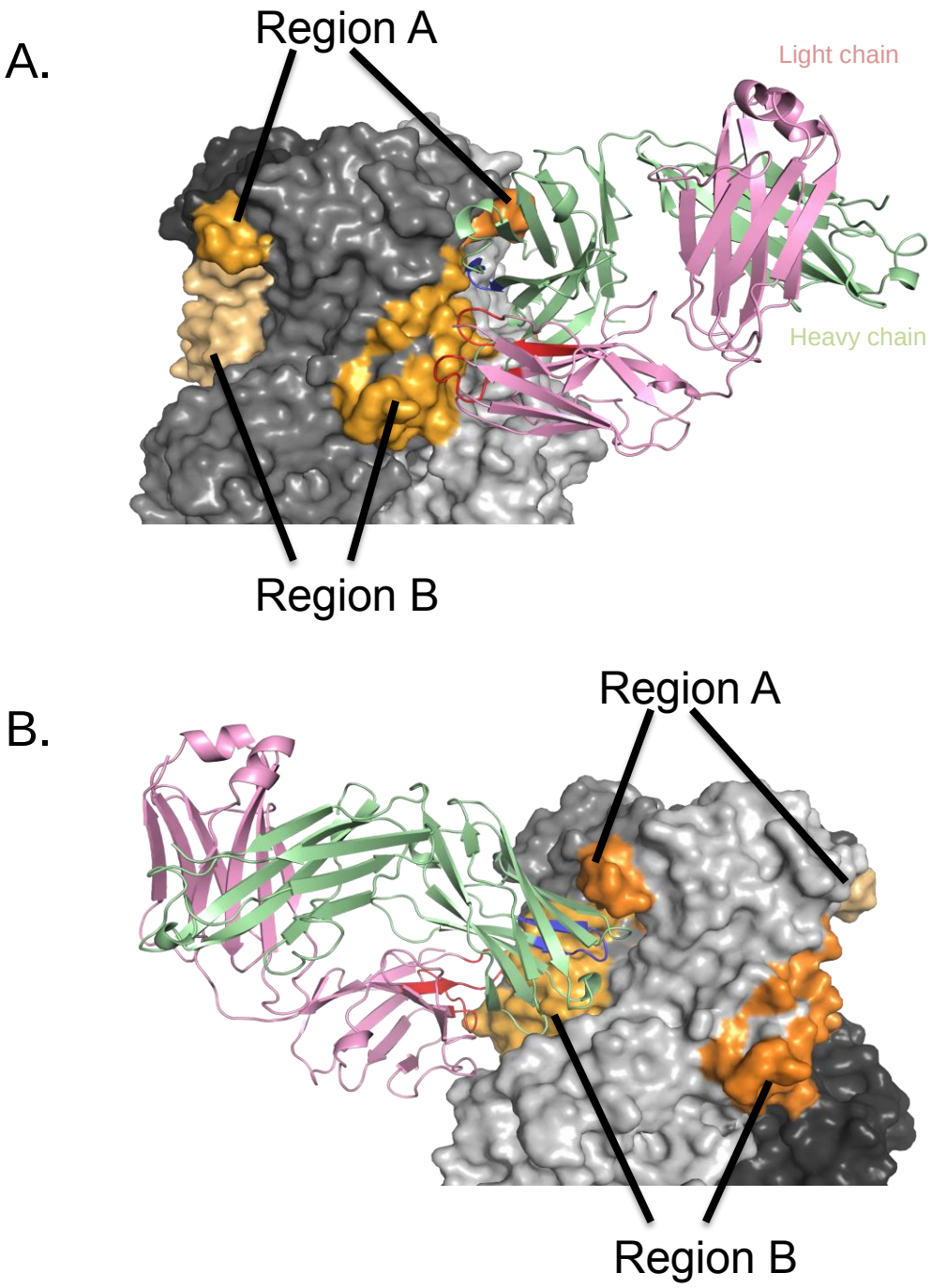

Figure 3-6: Computer-generated model of VP6-RV6-26 conformation and comparison to predicted epitope regions. The model was generated with RosettaDock, using DXMS-predicted epitope and paratope regions as restraints during docking. (A) RV6-26 bound to VP6 at a quaternary epitope made up of region A on one VP6 protomer and region B of a second VP6 protomer. Shades of gray represent the three protomers that make up the VP6 trimer, and the shades of orange represent the DXMS-predicted epitope regions mapped on each protomer. Heavy and light chains are pink and green, respectively. DXMS predicted paratope regions for heavy and light chain are colored violet and red, respectively. (B) Horizontal rotation of panel A.

A.

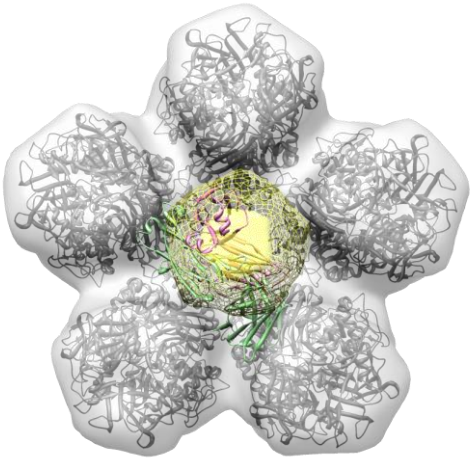

B.

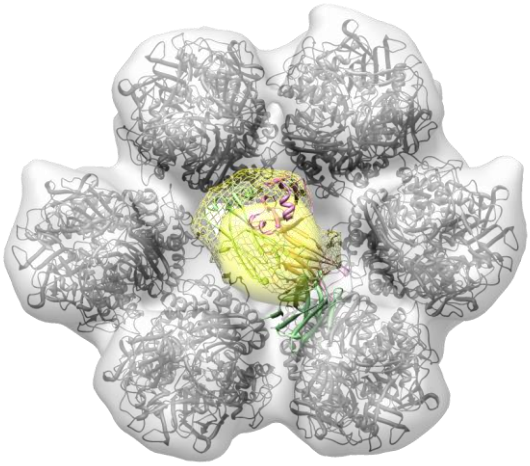

C.

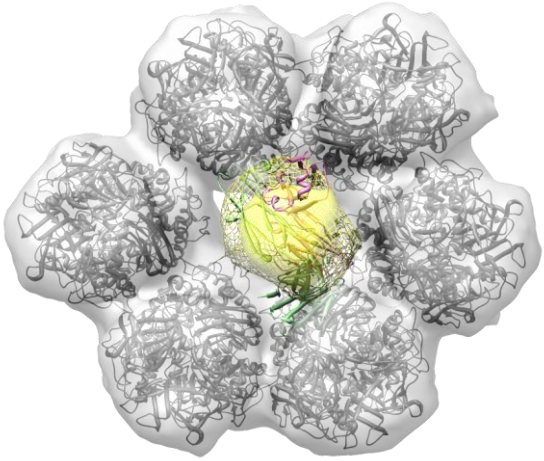

Figure 3-7: Computer-generated model of VP6-RV6-26 conformation and comparison to cryo-EM density maps. Fit of representative model into experimental and simulated cryo-EM density of Type I (A), II (B), & III (C) channels, respectively. Density attributed to Fab is yellow with simulated Fab density shown as mesh. Experimental VP6 density is gray (simulated density not shown). Cryo-EM density is overlaid on VP6 crystal structure (3KZ4 (43)). Fab interacting with a single VP6 trimer is displayed as cartoon with light chain colored pink and heavy chain colored green.

Binding of RV6-26 Fab does not induce a conformational change to the DLP structure such that it mimics VP7 binding to VP6 in the mature virus. We next investigated the structural impact of binding of RV6-26 to VP6 in the Type I channels. We considered two possibilities regarding the structural effects. One model was that the antibody sterically blocks the channel through which RNAs traffic. The other possibility was that binding of RV6-26 Fab to DLP might induce a conformational change to the global structure of the VP6 layer, such that the bound structure resembled the change this layer undergoes upon VP7 binding during rotavirus assembly, specifically at the five-fold symmetrical transcriptional pore (12). To investigate these possibilities, we fitted atomic models derived from a crystallographic study of DLP (PDB-ID 3KZ4) or a cryo-EM study of TLP (infectious rotavirus particle; PDB-ID 3N09; (12) into the cryo-EM density of the RV6-26-DLP complex. These two coordinate sets differ in that the TLP coordinates display a tighter ring of 5 VP6 trimers as well as a narrower Type 1 channel within the ring of five VP6 trimers at the 5-fold axis. The assessment of the RV6-26-DLP conformation involved fitting coordinates for the ring of five VP6 trimers from the DLP or TLP to the corresponding RV6-26-DLP cryo-EM density segment with the Fit-In-Map feature of Chimera software. The idea behind this test was that it would be easier to distinguish between the fit of the two types of VP6 trimer rings than it would be to accurately measure the diameter of the transcriptional pore given the resolution of the RV6-26-DLP cryo-EM structure (10.9 Å). To validate the accuracy of the fitting function for comparison of RV structures, we first placed either the DLP or TLP coordinate sets into a density segment from a cryo-EM structure of DLP (Figure 3-8 A) or a cryo-EM structure of a VP7 recoated DLP (Figure 3-8 B). As expected, a higher fitting correlation

was observed with DLP coordinates into the DLP density map and with TLP coordinates into the VP7 recoated DLP density map. Next we determined whether the arrangement of VP6 molecules at the Type I channel within the RV6-26 Fab-DLP complex most resembled DLP or the conformationally-altered arrangement found in TLPs. We found a higher fitting correlation of the DLP coordinate set to the RV6-26-DLP complex (Figure 3-8 C). This result indicates that binding of the RV6-26 Fab does not induce a conformational change in the ring of five VP6 trimers at the five-fold axis of the DLP. In addition, we also converted the coordinates for a ring of five VP6 trimers at the 5-fold axis from the DLP and TLP atomic resolution structures into density maps at 10.9 Å resolution to simulate the cryo-EM density. Fitting of these two simulated density maps for a ring of five VP6 trimers into the cryo-EM structure of the RV6-26-DLP complex also indicated a better fit for the DLP structure. Therefore, the data suggest a mechanism of inhibition of the transcriptional pore is steric hindrance of the pore, rather than induced conformational change.

RV6-26 covers an important area of electrostatic charge on VP6 that may be critical for mRNA transport. Poisson-Boltzmann analysis of VP6 and Fab provided a profile of the electrostatic surface of both proteins. Both paratope regions in the heavy and light chains resided in positively-charged regions of the Fab surface (Figure 3-9 A). The DXMS-identified epitope recognized by RV6-26 includes a patch of negatively-charged surface at the bottom of the trimer, close to the VP2 layer, inside which transcription occurs (Figure 3-9 B). Atomic resolution structures from bluetongue virus suggest a role for the surface charge of the transcriptional pore, where positively-

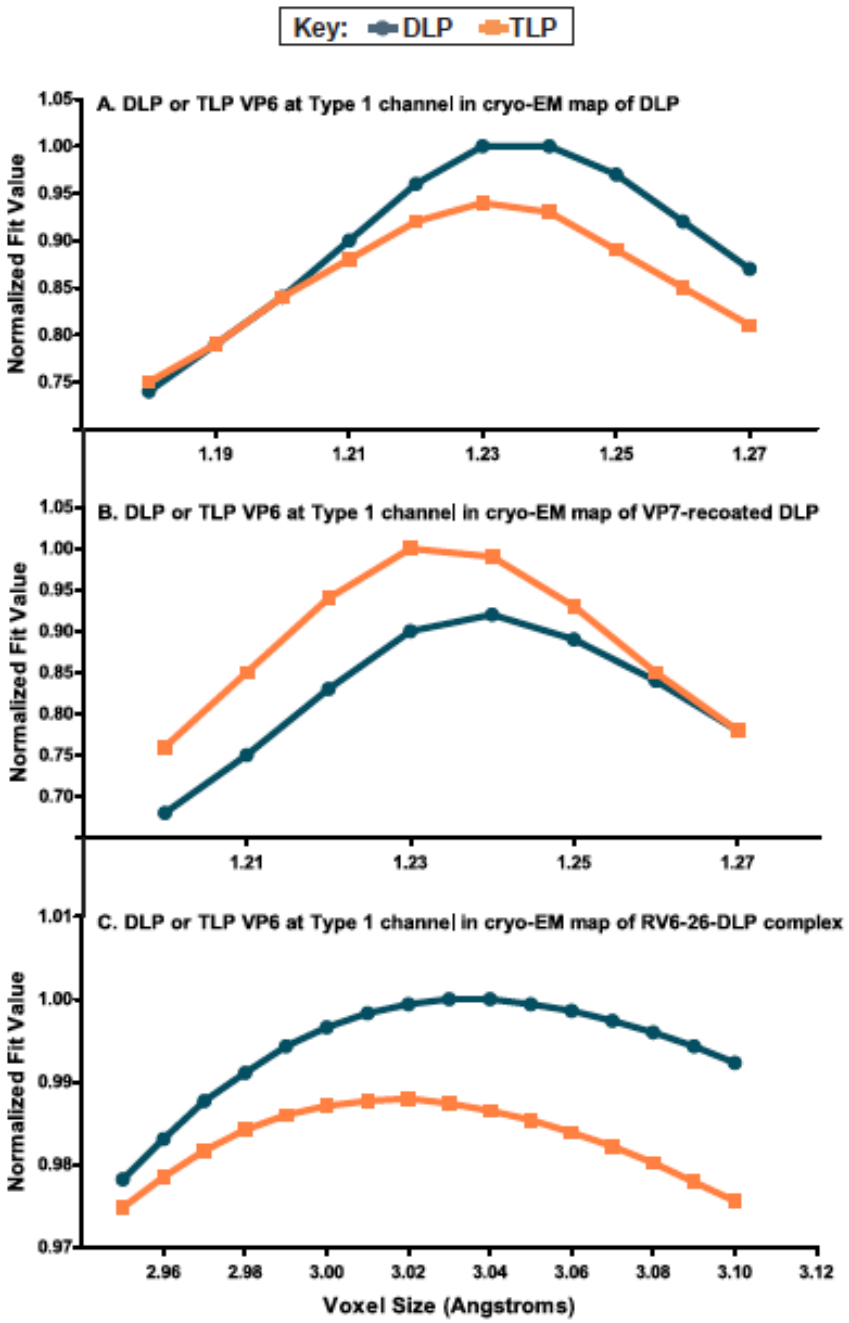

Figure 3-8: Docking of coordinates for a ring of five VP6 trimers at the Type I channel into cryo-EM maps of DLP, VP7 recoated DLP, and the RV6-26-DLP complex. (A) Coordinates for a ring of five VP6 trimers, extracted from the crystal structures of the rotavirus DLP (PDB-ID 3KZ4, blue) and the infectious rotavirus particle (PDB-ID 3N09, orange), docked into a segment of the DLP cryo-EM structure (EM Data Bank EMD-1460). (B) Same coordinates docked into a segment of the VP7 recoated DLP cryo-EM structure (EM Data Bank EMD-1571). (C) Same coordinates docked into a segment of the RV6-26-DLP complex cryo-EM structure. The voxel sizes of the cryo-EM density maps (1.205 Å/voxel for DLP and VP7 recoated DLP; 3.02 Å/voxel) were varied plus or minus a few percent to find maximum fit values. Fit values were reported by the UCSF Chimera Fit-In-Map function and are shown normalized in each panel.

charged residues in the core layer are positioned to attract negatively-charged nascent mRNA to the mouth of the pore for extrusion (14). The electrostatic repulsion between the net negative charge of the five-fold channel surface of RV and the viral mRNA is thought to facilitate egress of the mRNA transcript by increasing its fluidity (42). It is apparent that binding of RV6-26 to its epitope likely would inhibit RV transcription (42). Binding of RV6-26 to its epitope could partially inhibit RV transcription by covering one of the five negatively-charged patches within the Type I channel. It is of interest that this negatively-charged patch of residues in the channel is highly conserved among diverse RV strains.

Discussion

Structural studies using single particle cryo-EM provided insights into the mechanism of inhibition of RV transcription by RV6-26. A previously published high-resolution cryo-EM study of uncoating and recoating of the outer VP7 layer showed a distinct shift in the orientation of the VP6 trimers around the five-fold axes that resulted in a 5 Å decrease in diameter of transcription pore (12). It was suggested that the uncoating of the VP7 layer in the transcriptionally-incompetent RV particle, and ensuing reorientation of the five-fold VP6 trimers, could serve as a trigger for the activation of RNA synthesis. Previous cryo-EM studies of murine inhibiting or non-inhibiting Fabs postulated either prevention (66) or induction (33) of a conformational change in the VP6 trimers at the transcriptional pore in the inhibiting Fab-complex structures in a similar way as that mediated by VP7. One of the studies suggested no effect of inhibitory Fab binding on DLP conformation (66). The cryo-EM structures obtained in those Fab

A.

B.

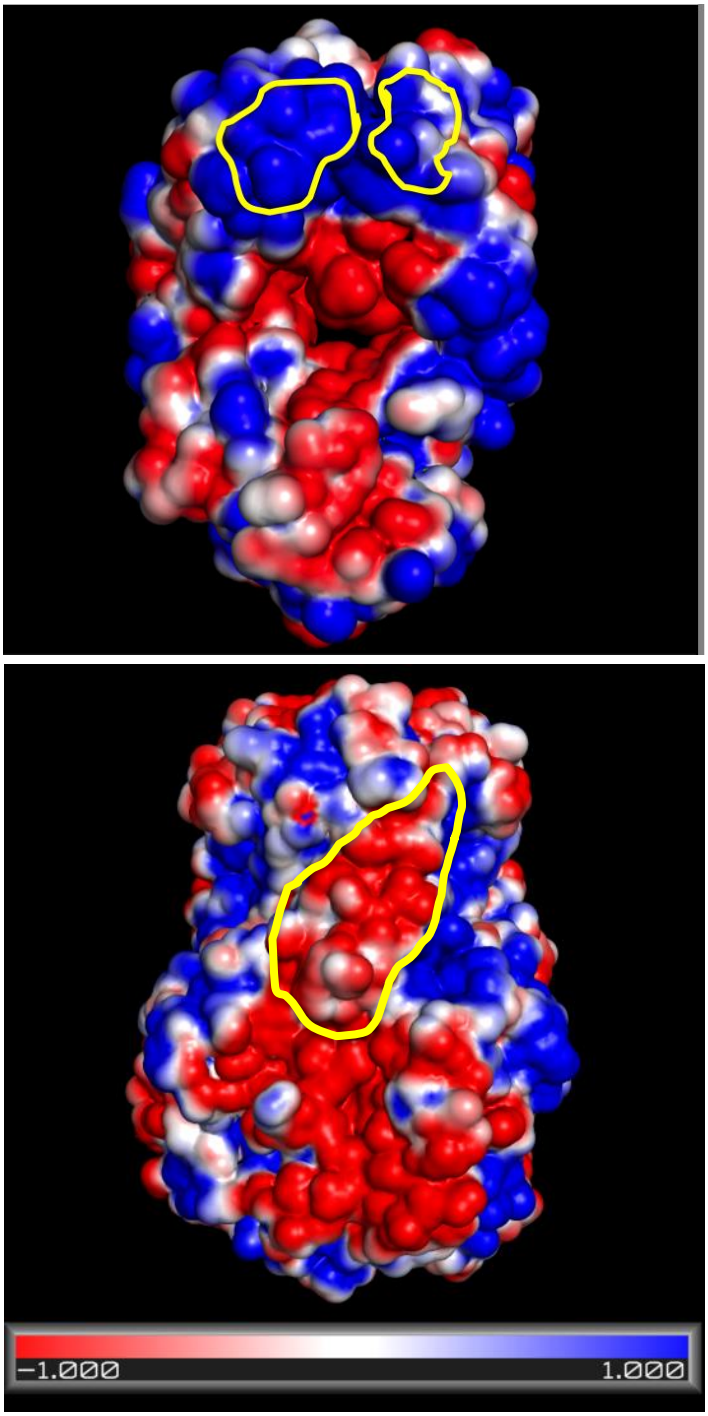

Figure 3-9: Electrostatic analysis of the binding surfaces involved in interaction between RV6-26 Fab and VP6. The surface electrostatic potential of the VP6 trimer (A), lateral view, or the RV6-26 Fab (B), with red or blue for negative or positive charges, respectively. The yellow circles indicate region B of the VP6 epitope (A) and the heavy and light chain elements of the paratope on Fab RV6-26 (B), as defined by DXMS analysis.

studies, however, likely were not high enough resolution to definitively resolve whether or not a conformational change resulted from binding.

In this study, we did not observe any conformational changes to the five-fold VP6 trimers as a result of RV6-26 binding that resembled those induced by VP7 recoating. Our RV6-26-DLP complex structure showed that the Fab bound to the VP6 trimers with Fab projecting into the center of the Type I channel (transcriptional pore), suggesting a physical blockade of the pore as the principal mode of inhibition. We determined the epitope of the RV6-26 Fab by DXMS and computational docking using Rosetta, which revealed a quaternary epitope involving an inserted β-hairpin of one VP6 protomer and some pore-exposed residues within a β-sheet of the adjacent VP6 protomer comprising residues 231-260 and 265-292, respectively. The data here indicating the quaternary nature of epitopes recognized by inhibitory human Fabs is consistent with some previous epitope mapping studies of murine inhibitory Fabs. The main difference observed between the inhibiting and non-inhibiting Fab was in the location of their epitopes (66). The epitope of inhibitory Fabs involved multiple loops on two VP6 protomers, while only one VP6 protomer was involved in binding of the non-inhibitory Fabs. The light chain inserted deeper into the transcription pore, while the heavy chain bound to a region higher up in the pore. Our previous mutagenesis work showed that the HCDR2 loop of RV6-26 is associated with much of the antibody inhibitory function (27).

Electrostatic analysis of the surface of the RV6-26 epitope and paratope revealed that the epitope lies within a patch of negatively-charged surface that extends from the base of VP6 towards the bottom of the transcriptional pore. It has been postulated that this negatively-charged surface within the transcription channel may be important for

repulsion of negatively charged viral mRNA during egress from the particle, as transcription is initiated within the RV-DLP. Successful threading of an initiated mRNA transcript through the pore may be a critical step required for the transition from transcription initiation to elongation, which is essential for RV to produce mature full-length transcripts (33). Not surprisingly, the paratope surface of RV6-26 is very positively charged, suggesting that the antigen-antibody interaction may be driven by electrostatic interactions between the antibody and VP6. It is possible that RV6-26 binding to VP6 partially disrupts a charged-based mechanism of guidance of the path of mRNA translocation from the particle core, however this study did not specifically address the mechanism of RNA threading. The size of the Fab in the Type I channel likely is sufficient to sterically block RNA egress from the channel even if the charge determinants are not essential to replication.

These studies also revealed a pattern of epitope recognition that provides insights into the overall viral architecture, and may have broad implications for antibody recognition of epitopes in the context of whole viral particles. RV6-26 exhibited three different binding patterns at the Type I, II and III channels. Interestingly, reconstructed density in the Type III channel was asymmetric, suggesting tighter interactions with VP6 trimers adjacent to the five-fold or three-fold trimers. However, we demonstrated that this asymmetry can be explained by the deviation from a perfect hexagonal pore at the quasi-six-fold axes. This observation does not exclude preferential binding or differential accessibility resulting from this deviation from perfect symmetry. However, neither effect is needed to explain our findings at the resolution of the data.

Chapter Summary

Data from chapter II indicate that the RV6-26 Fab engages a quaternary epitope that lies mainly on the lateral side of the VP6 molecule. Based on the orientation of the epitope, I sought in this chapter to determine the mechanism of antiviral activity of the RV6-26 Fab. Cryo-EM provided an appropriate technique to achieve this goal in a way that would not be possible from determining the epitope. The cryo-EM structure reveals that RV6-26 binds directly in the middle of the transcription pore. Secondly the modeling studies show that only one Fab can bind to any VP6 trimer within the pore, and it is enough to block the channel. Finally, the cryo-EM analysis shows that no conformational change is induce upon Fab binding. Collectively, the cryo-EM structure of the RV6-26-DLP complex, combined with the deuterium exchange mass spectroscopy evaluation of the epitope regions and modeling of the docked Fab fragment crystal structure together indicate that the predominant mode of rotavirus inhibition by RV6-26 is steric hindrance of the DLP transcriptional pore.

CHAPTER IV

QUASI-EQUIVALENT NATURE OF VP6 TRIMERS ON RV-DLP AS REVEALED BY BINDING OF RV6-25 FAB

Introduction

RV6-25 is an antibody that was previously isolated in our lab that also uses the V_H1-46 immunodominant gene segment. However, it does not inhibit RV transcription in *in-vitro* studies (27). It is interesting to note that RV6-25 shares the same germline as the highly inhibitory RV6-26.

In the previous chapter, I elucidated the mechanism by which RV6-26 mediates it antiviral activity. Since it shares a similar germline with RV6-25, it is interesting to investigate the structural basis of the lack of antiviral activity of RV6-25. Even though RV6-26 has a significantly higher binding affinity to DLP when compared to RV6-25, the affinity of RV6-25 is high enough that should be able to mediate viral inhibition. Antibodies with similar affinities have been shown to neutralize virus (30).

In this chapter, I describe the structural basis of lack of viral inhibition by RV6-25 using the cryo-EM structure of RV6-25 bound to DLP. We determined the epitope of the RV6-25 antibody using DXMS. Furthermore, the complex structure informs on subtle differences in the VP6 trimers that make up the outer layer of the DLP.

Materials and methods

Expression and purification of recombinant RV6-25 Fab. The isolation of the genes encoding the human VP6-specific monoclonal antibody RV6-25 from a single B cell was described previously (70), and the antibody gene sequences are available in GenBank, accession numbers AF452995 and AF453155 for the variable heavy and light chains, respectively. The RV6-25 heavy and light chain variable region genes were sequence-optimized and synthesized as cDNAs (GeneArt, Regensburg, Germany). These synthetic genes were cloned into the pEE6.4 expression vector (Lonza) in-frame with a mouse kappa chain leader sequence at the 5′ end and optimized C_L and C_H1 constant domain sequences at the 3′ end, to encode a fully human Fab antibody fragment without affinity tags. The separate plasmids encoding heavy or light chain genes each were transformed into DH5α strain *E. coli* cells for large-scale plasmid DNA preparation (PureYield; Promega). Heavy- and light-chain encoding plasmid DNAs were co-transfected transiently into a high-producing clonal variant of the HEK-293 cell line cells (FreeStyle™ 293-F cells; Invitrogen) using Polyfect reagent (Qiagen). The 293-F cells were grown in FreeStyle 293 serum-free expression medium (Invitrogen) in shaker flasks at 125 rpm and 8% CO_2 for 7 days. The culture supernatant was collected on day 7 and purified by fast protein liquid chromatography using an ÄKTA FPLC™ device and HiTrap KappaSelect column (GE Healthcare) in D-PBS, and then concentrated with 30 mL Amicon Ultra centrifugal filter units with 30 kDa molecular weight cut-off (Millipore).

Preparation and purification of rotavirus double-layered virus particles (DLPs). A strain of rhesus rotavirus (RRV) was kindly provided by Susana López (Universidad Nacional Autónoma de México). MA-104 cells (CRL-2378.1; ATCC, Manassas, VA) were used to propagate rotavirus to make DLPs. They were grown in complete medium (CM) consisting of DMEM with 4.5% glucose (Mediatech) supplemented with 10% (v/v) fetal bovine serum (Invitrogen), 0.1 mM MEM non-essential amino acids (Invitrogen), 100 I.U./mL penicillin, 100 µg/mL streptomycin, 2 mM glutamine and 1 mM sodium pyruvate (all from Mediatech). Infection medium (IM), used when cells were inoculated with rotavirus and cultured, contained all of the above supplements except serum, and trypsin-EDTA (Invitrogen) was added to a final concentration of 1 µg/mL. RRV was inoculated onto cell culture monolayers of the MA-104 cells at low MOI. When cell monolayers exhibited significant cytopathic effect (typically after 48 hrs), the supernatant and cell fractions were collected and virus was isolated by ultracentrifugation in a Sorvall Discovery 90SE centrifuge with a Surespin 630 rotor at 20,000 rpm for 1.5 hours at 4 °C. The resulting pellet was resuspended in Earle's Balanced Salt Solution (GIBCO®) and the cellular debris was removed by addition of 1,1,2-trichloro-trifluoroethane (EMD Chemicals) and blending. The suspension then was centrifuged at 2,000 rpm for 0.5 hours at 4 °C to separate virus from cell debris. Virus particles then were collected and purified by ultracentrifugation through a CsCl cushion at 20,000 rpm for 1.5 hours. To prepare concentrated DLPs, the collected viral particles were treated with 10 mM EGTA (Lonza) for 5 minutes at room temperature to remove the outer VP4 and VP7 protein layers of the rotavirus triple-layered particles. The resulting DLPs were purified further by CsCl density gradient ultracentrifugation at 29,700 rpm for 20 hours. The visible band

containing DLPs was collected and concentrated further by ultracentrifugation in the same CsCl density gradient at 29,700 rpm for 2 hours. The band then was collected and dialyzed into Tris-buffered saline (Mediatech).

Cryo-electron microscopy. These studies were performed in collaboration with Phoebe Stewart's laboratory in the Department of Molecular Physiology and Biophysics. Purified DLPs were mixed with five-fold molar excess of purified RV6-25 Fab protein, and then the excess antibody was removed using centrifugal filters with Sephadex G-50 resin. The complexes of RV DLPs with RV6-25 Fab in Tris-buffered saline pH 8.0 with 0.5% glycerol were applied to freshly prepared electron microscopy (EM) grids with a holey carbon film. The excess liquid from a 2-3 μL droplet was blotted away with filter paper. Another 2-3 μL droplet was added to the same EM grid and excess liquid was blotted as before. The sample grid was plunged immediately into liquid ethane cooled by liquid nitrogen. All data was collected on an FEI Tecnai Polara microscope equipped with a field emission gun (FEG) operating at 300 kV in nanoprobe mode. The sample grids were maintained at liquid nitrogen temperature during data acquisition. Images were recorded digitally on a Gatan UltraScan 4000 (4k x 4k) CCD camera. Micrographs were collected with a defocus range of 0.5 - 5 μm and with an absolute magnification of 199,000x.

Image processing and reconstruction. Individual particle images were centered manually, cropped and binned using in-house scripts in conjunction with IMAGIC and EMAN image processing suites. A total of 1, 062 particle images was picked and processed in this dataset. Images were binned and stacked with 6.0 Å pixel sizes. The stacks were used

for initial CTF parameter determination using CTFFIND3 and CTFREFINE. Orientation, magnification and defocus parameter determination and refinement were carried out using FREALIGN. Image processing was carried out through 10 rounds of FREALIGN refinement; converging at a resolution of 21.5 Å. Resolution was determined as measured by the Fourier shell correlation (FSC) 0.5 criterion. Icosahedral symmetry was imposed during data processing.

VP6 head domain purification and expression. A DNA copy of the VP6 sequence encoding residues 147 – 339 was amplified from a full-length VP6 DNA construct by polymerase chain reaction (PCR) with Pfu Ultra polymerase (Stratagene) using the following primers:

Forward: 5´-GGAAGGccatggccCGGACCGGCTTCACCTTCCAC-3´

Reverse: 5´- GTGGTGctcgagGCTGGCGTCGGCCAGCACGC-3´

The PCR product was cloned into the pET28a vector (Novagen) using the NcoI and XhoI restriction sites. For expression and purification, the pET28a vector containing the head domain construct was transformed into BL21(DE3) *E. coli* strain. Cells were grown in 1 L of LB medium to an OD_{600} of 0.6 and protein expression then induced by addition of IPTG to a final concentration of 0.1 mM and allowed to grow overnight at 20 ºC. Cells were harvested by centrifugation and disrupted with a French pressure cell press in 50 mM sodium phosphate buffer, pH 8.0. The soluble fraction was clarified and applied over a Ni-NTA column. The VP6 protein then was eluted with the above buffer with 400 mM imidazole. The eluate was concentrated in Amicon Ultra filter tubes (Millipore) and passed through a Superdex S200 column for additional purification.

Hydrogen deuterium exchange mass spectrometry (DXMS). These studies were performed in collaboration with Virgil Wood's laboratory at University of California, San Diego. We performed comparative DXMS studies with the VP6hd construct alone or with VP6hd in complex with RV6-25 Fab, as previously described in chapter II. Briefly, quench conditions optimal for maximum peptide fragmentation were determined prior to the deuteration experiments, as previously described (24, 37). Complexes of VP6hd and Fab were prepared by mixing VP6hd and RV6-25 Fab at 1:1.4 stoichiometric ratio, and incubating the mixture at 0 °C for 30 minutes.

Functional hydrogen-deuterium exchange reaction of free VP6hd was initiated by diluting 0.7 μL of stock solution into 1.3 μL of H_2O buffer (8.3 mM Tris, 150 mM NaCl, in H_2O, pH 7.15), and then mixed with 6 μL of D_2O buffer (8.3 mM Tris, 150 mM NaCl, in D_2O, pD_{READ} 7.15). At 10 sec, 100 sec or 1,000 sec, 12 μL of optimized quench reagent (0.8M GuHCl in 0.8% formic acid) was added to the respective samples and then samples were frozen at -80 °C. The functionally-deuterated antibody-bound VP6hd samples were prepared by diluting 1.5 μL of complex solution (9.2 mg/mL) into 0.5 μL of non-deuterated buffer, and then mixed with 6 μL of D_2O buffer (8.3 mM Tris, 150 mM NaCl, in D_2O, pD_{READ} 7.15). At 10 sec, 100 sec or 1,000 sec, 12 μL of optimized quench reagent was added to the respective samples and then samples were frozen at -80 °C. In addition, non-deuterated samples (incubated in H_2O buffer mentioned above) and equilibrium-deuterated back-exchange control samples (incubated in D_2O buffer containing 0.5% formic acid overnight at 25 °C) were prepared as previously described (24, 37, 40). Later, the samples were thawed automatically on ice and then immediately passed over an AL-20-pepsin column (16 μL bed volume, 30 mg/mL porcine pepsin

(Sigma)), which was run at a flow rate of 20 μL/min with 0.05% trifluoroacetic acid. The resulting peptides were collected on a C18 trap and separated using a C18 reversed phase column (Vydac) running a linear gradient of 0.046% (v/v) trifluoroacetic acid, 6.4% (v/v) acetonitrile to 0.03% (v/v) trifluoroacetic acid, 38.4% (v/v) acetonitrile over 30 min with column effluent directed into an LCQ mass spectrometer (Thermo-Finnigan LCQ Classic) for epitope mapping. Data were acquired in both data-dependent MS:MS mode and MS1 profile mode. SEQUEST software (Thermo Finnigan Inc.) was used to identify the sequence of the peptide ions. The centroids of the isotopic envelopes of non-deuterated, functionally-deuterated, or fully-deuterated peptides were measured using DXMS Explorer (Sierra Analytics Inc., Modesto, CA), and then converted to corresponding deuteration levels with corrections for back-exchange (80).

Results

RV6-25 binds to the apical surface of VP6 molecules on DLPs. RV6-25 and RV6-26 are very closely related and share the same variable gene segment (71). However, RV6-26 inhibits viral transcription, whereas RV6-25 does not (27). I determined the pattern of binding of RV6-25 to DLPs using cryo-electron microscopy (cryo-EM) reconstruction (Figure 4-1 A-B), to determine the structural basis for the inability of the antibody to inhibit RV. The reconstruction of the Fab-DLP complex was computed from 1, 062 complex particle images extracted from corresponding cryo-EM micrographs. The estimated final resolution of the RV6-25-DLP complex is 21.5 Å, using the 0.5 FSC criterion (Figure 4-1 C). Like most cryo-EM structures that have been determined for icosahedral viral particles in complex with antibodies and receptors (51), RV6-25 Fab

protrudes from the VP6 trimers and extends away from the viral surface in a regular pattern depending on the position of the VP6 trimer in the VP6 layer (Figure 4-1).

RV6-25 Fabs bind to all available VP6 epitopes around the type I channels. All the VP6 trimers around the five-fold axis (type I channel) were bound by three Fab molecules each, occupying all the available binding epitopes. However, the Fab densities that project into the type I channel are not visible at higher thresholds because of the imposed icosahedral averaging during reconstruction of the complex structure (Figure 4-2 A-B). At a lower threshold, an averaged density of bound Fabs that project into the transcription pore is visible (Figure 4-1 B). A Fab model of RV6-25 fits into the cryo-EM density with a cross coefficient correlation of 0.9217 (Figure 4-2 C) using the Chimera Fit-In-Map function. The inner VP2 layer of the DLP has a T=2 architecture that surrounds the viral genomic material, whereas the intermediate VP6 layer of the viral particle has a T=13 icosahedral symmetry. Because of the symmetry mismatch between the VP2 and VP6 layers, five distinct VP6 trimer positions exist on the DLP outer layer, designated P, P′, T, T′ and D (43). The P trimers surround the five-fold axis and form the type I channel (Figure 4-2 B). The RV6-25 Fab densities bind at an angle to the P trimers such that they project out to the adjacent channel and over adjacent trimers. These structural features immediately suggest the difference in epitope when compared to the RV6-26 structure in chapter III, where the Fabs appear to fit directly over the center of the type I channel.

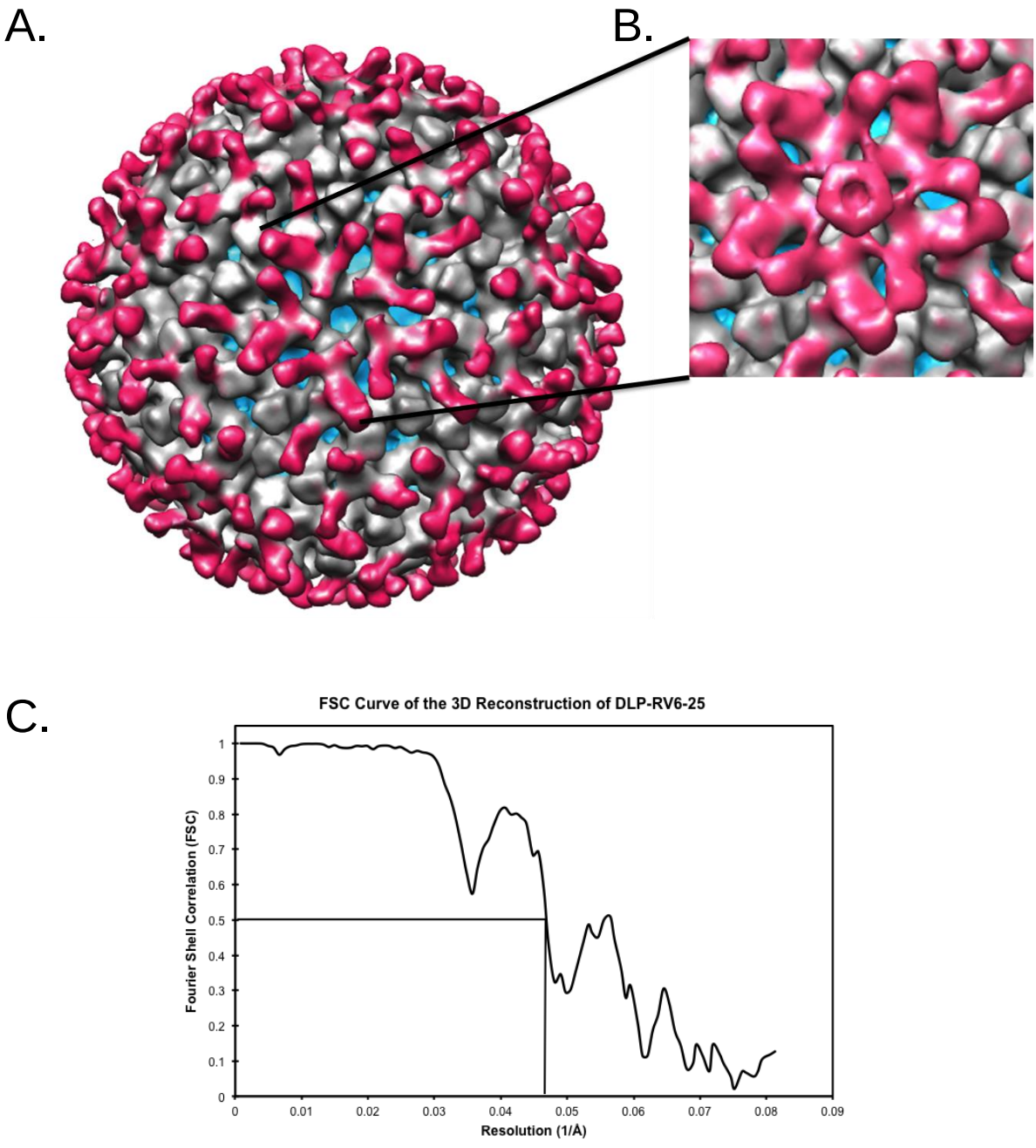

Figure 4-1. 3D reconstruction of the RV6-25-DLP complex to a resolution of 21.5 Å. (A). Surface representation of the structure of RV6-26-DLP complex. The VP2 layer is colored cyan, the VP6 layer is colored gray, and the Fabs are colored pink. (B.) Magnification of the type I channel at lower threshold showing additional density that represents the third Fab molecule bound to a VP6 trimer. (C). FSC curve of the complex reconstruction showing FSC 0.5 resolution at 21.5 Å.

RV6-25 Fabs bind to only one of the available Fab epitopes on the P′ trimers around the type II channels. Two of the P trimers form part of the type II channels that surround all the type I channels on the surface of the VP6 layer. The binding angle of the Fabs to the P VP6 trimers in the type I channel (Figure 4-3 A-B) precludes full occupancy of the available epitopes on the adjacent P′ trimers. The obstructed availability of the Fab epitopes on the P′ trimers allows for binding only to the epitopes where the Fab densities are oriented towards the two- and three-fold icosahedral axes (Figure 4-3 A-B). Interestingly, no Fabs bound to the D or T′ trimers adjacent to the two-fold or three-fold axis, respectively. The D and T′ trimers, together with two P and P′ trimers each, form the type II channels (Figure 4-3 B). Indeed, fitting of a RV6-25 Fab model into one of the Fab densities bound to the P' trimers yielded a cross correlation coefficient of 0.8707 using the Chimera Fit-In-Map feature (Figure 4-3 C).

RV6-25 Fabs bind to all Fab epitopes on the three-fold trimers. The icosahedral symmetry of the DLP places a trimer, T, directly at the three-fold axis (43). The complex structure shows that all the available Fab epitopes on the T trimer were occupied by Fabs that roughly lie along the three-fold axis in the type III channel (Figure 4-4 A-B). The P′ trimer that is also part of the type III channel shows a bound Fab density oriented towards the two-fold symmetry similar to the orientation of the Fab bound to the P' trimers in the type II channel. Furthermore, as in the type II channel the D and T′ trimers did not have

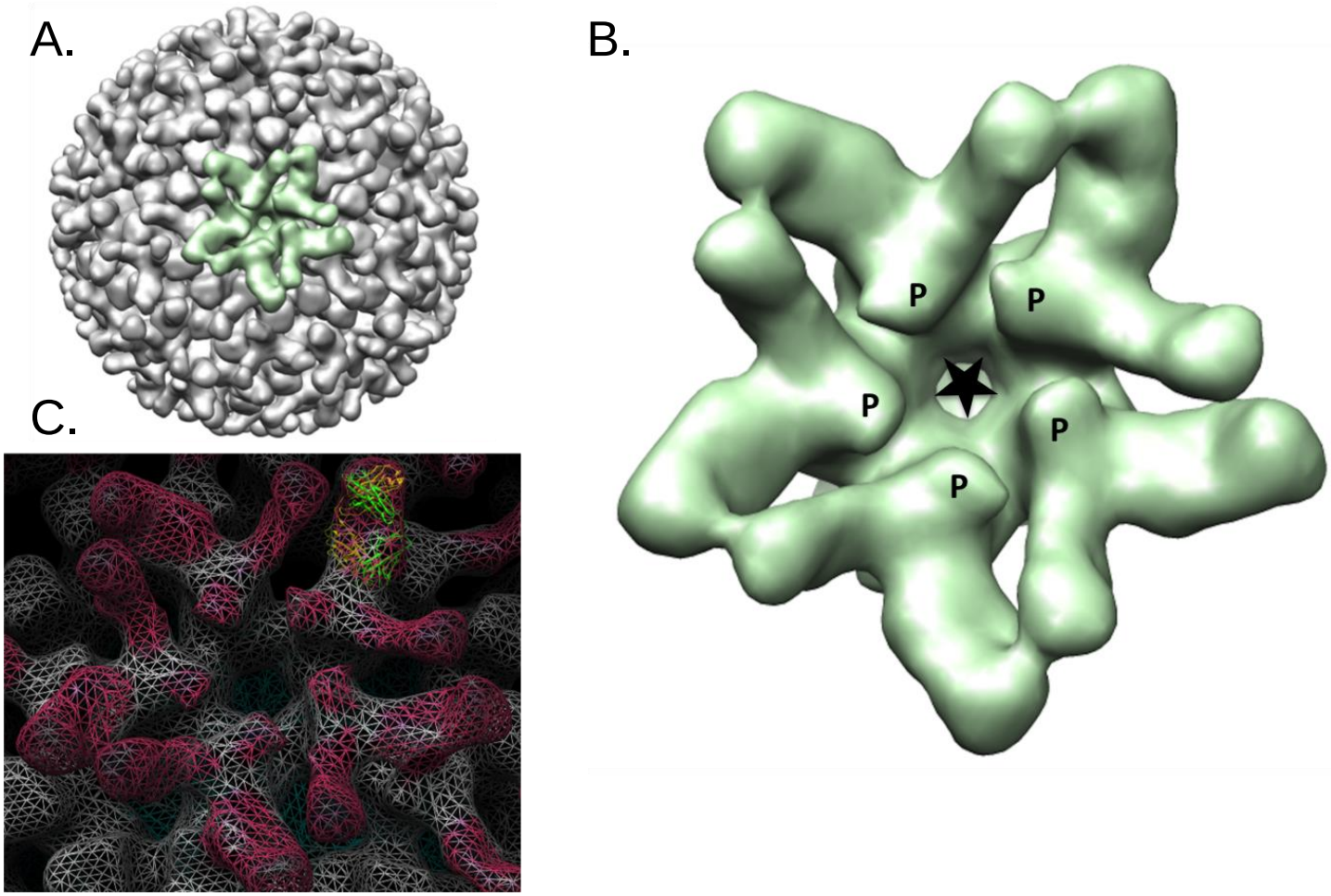

Figure 4-2. Binding of RV6-25 Fab to VP6 trimers at type I channel. (A) Surface representation of RV6-25-DLP complex particle, highlighting the RV6-25 Fabs bound to the VP6 trimers around the type I channel (green) in the context of the whole virion particle (gray). (B) Type I channel is extracted with the P trimers labeled. The star represents the icosahedral five-fold axis. (C). Mesh representation of the type I channel showing ribbon diagram of Fab model docked into the cryo-EM density, using Chimera Fit-In-Map feature. Green and yellow represent the Fab heavy and light chains, respectively.

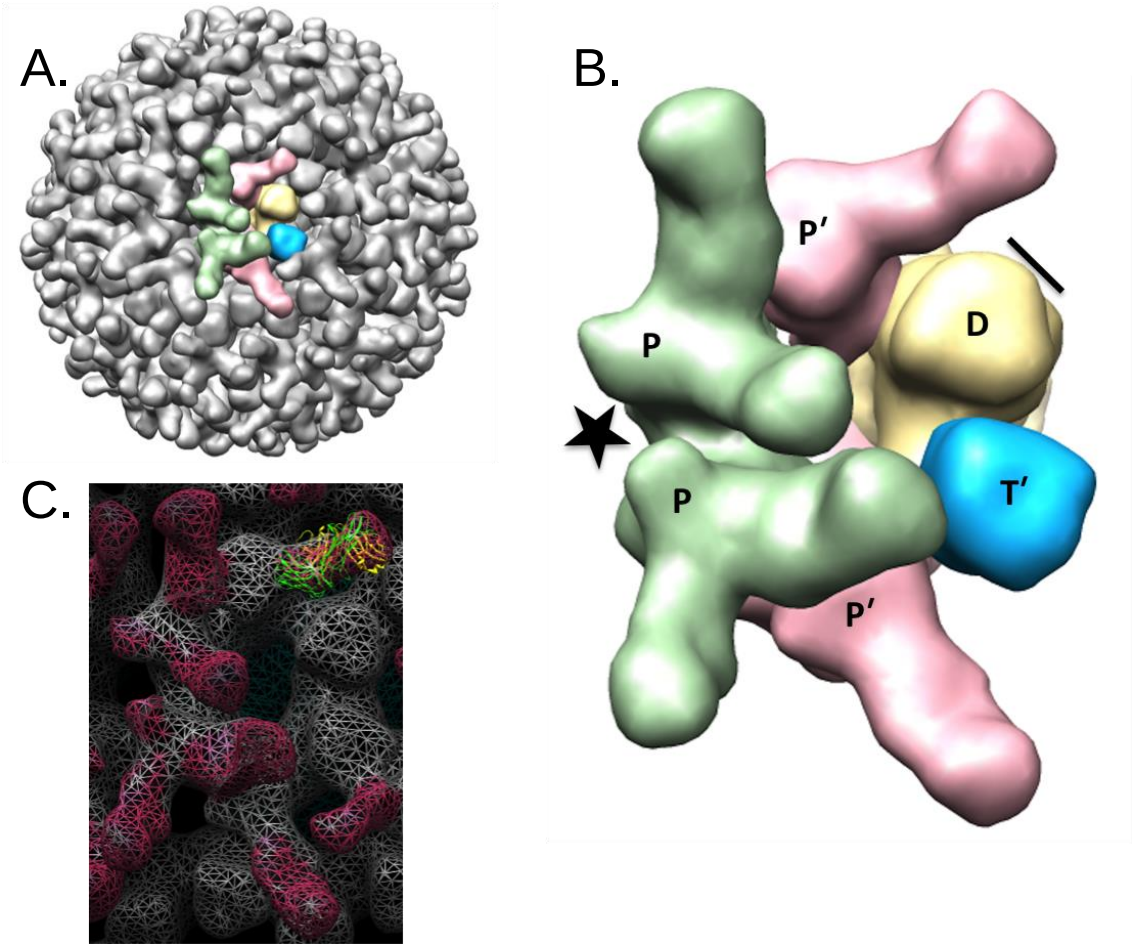

Figure 4-3. Binding of RV6-25 Fab to P' trimers at type II channel. (A) Surface representation of RV6-25-DLP complex particle, highlighting the RV6-25 Fabs bound to the VP6 trimers around the type II channel in the context of the whole virion particle (gray). (B) Type II channel is extracted with the distinct VP6 trimers colored and labeled. The star represents the icosahedral five-fold axis in the adjacent type I channel and the black line represents the two-fold axis (C). Mesh representation of the type II channel showing ribbon diagram of Fab model docked into the P' cryo-EM density using Chimera Fit-In-Map feature. The gray mesh represents the VP6 layer and the pink mesh represents the Fab density. Green and yellow represent the Fab heavy and light chains, respectively.

any bound Fabs (Figure 4-4 A-B). Taken into the context of all three channels, Fab binding to the epitopes on the distinct VP6 trimers is such that there are minimum steric clashes among the bound Fabs (Figures 4-5 A-B). Fitting of a Fab model into one of the Fab densities bound to the three-fold trimer showed a cross correlation coefficient of 0.8769 (Figure 4-4 C).

RV6-25 binds to an epitope on the apical loops of VP6. We sought to determine the precise residues of the epitope recognized by RV6-25. While the cryo-EM complex structure presents the possible contact surfaces of the Fabs to the VP6 trimers, the resolution is not high enough to determine the specific residues involved in the Fab-antigen interaction. Therefore, we employed enhanced amide hydrogen/deuterium exchange mass spectroscopy (DXMS) to define the residues that comprise the Fab epitope. Through DXMS, we identified peptides derived from regions including residues 197 – 214 (region 1) and 306 – 324 (region 2) to form the epitope of RV6-25 on VP6 (Figure 4-6 A). When labeled onto a ribbon map of the three dimensional structure of VP6 (PDB: 1QHD; (42)), it was clear that the epitope lies within the apical loops of the VP6 structure. Using the conventional nomenclature for jelly-roll motifs (58), region 1 spanned residues within the loop emanating from βB to βC (Figure 4-6 B-C). Region 2 extended from the loop emerging from the short αA helix down to βI (Figure 4-6 B-C). Taken into context with the orientation of the docked Fab in the cryo-EM density map, residues 197-214 and 308-316 in the loops between βB-βC; and the αA helix and βI are most likely directly involved in binding RV6-25 (Figure 4-6 B-C). The resolution of the DXMS technique does not allow for identification of individual contact residues.

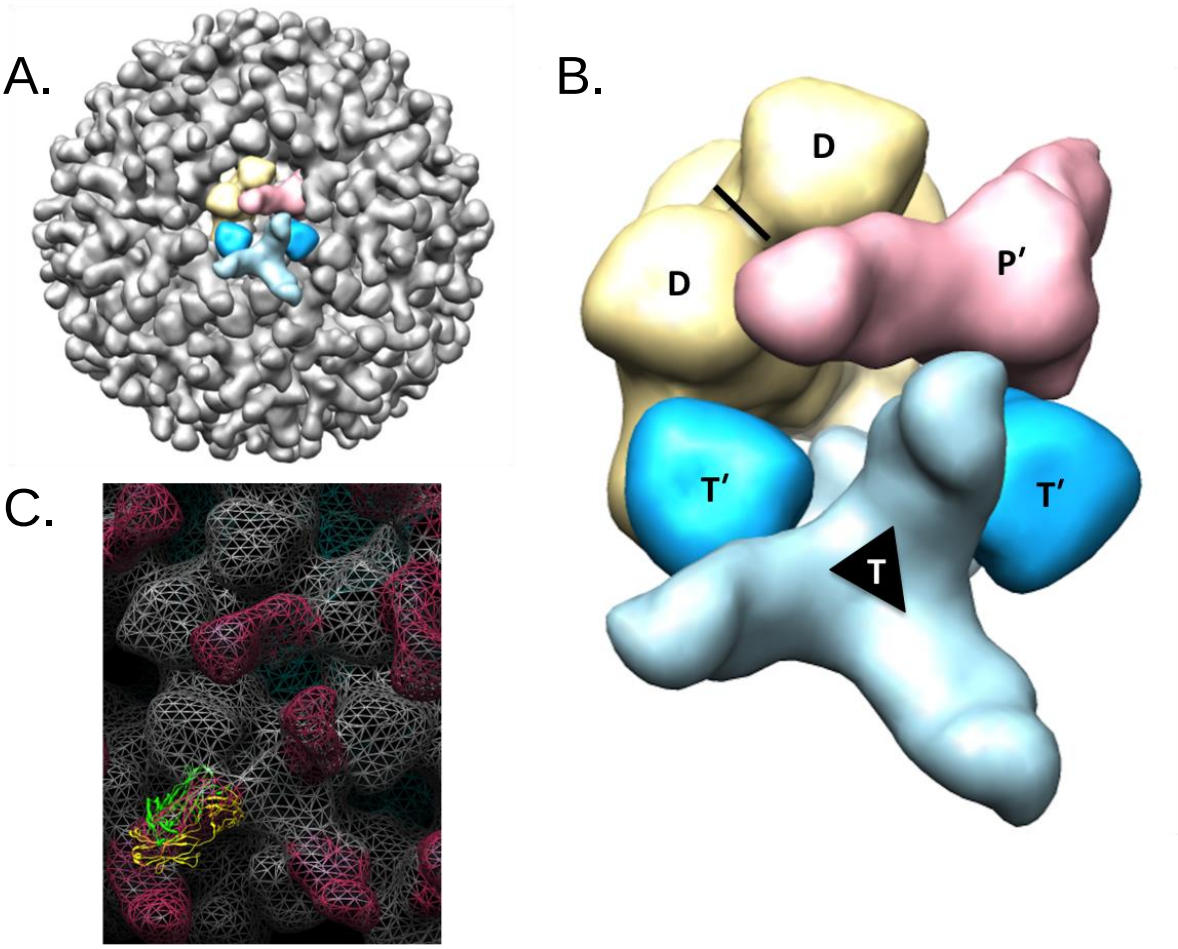

Figure 4-4. Binding of RV6-25 Fab to T trimer at the type III channel. (A) Surface representation of RV6-25-DLP complex particle, highlighting the RV6-25 Fabs bound to the VP6 T trimers around the type III channel in the context of the whole virion particle (gray). (B) Type III channel is extracted with the distinct VP6 trimers colored and labeled. The black triangle represents the icosahedral three-fold axis and the black line represents the two-fold axis (C). Mesh representation of the type III channel showing ribbon diagram of Fab model docked onto one of the T cryo-EM Fab-bound density using Chimera Fit-In-Map feature. The gray mesh represents the VP6 layer, and the pink mesh represents the Fab density. Green and yellow represent the Fab heavy and light chains, respectively.

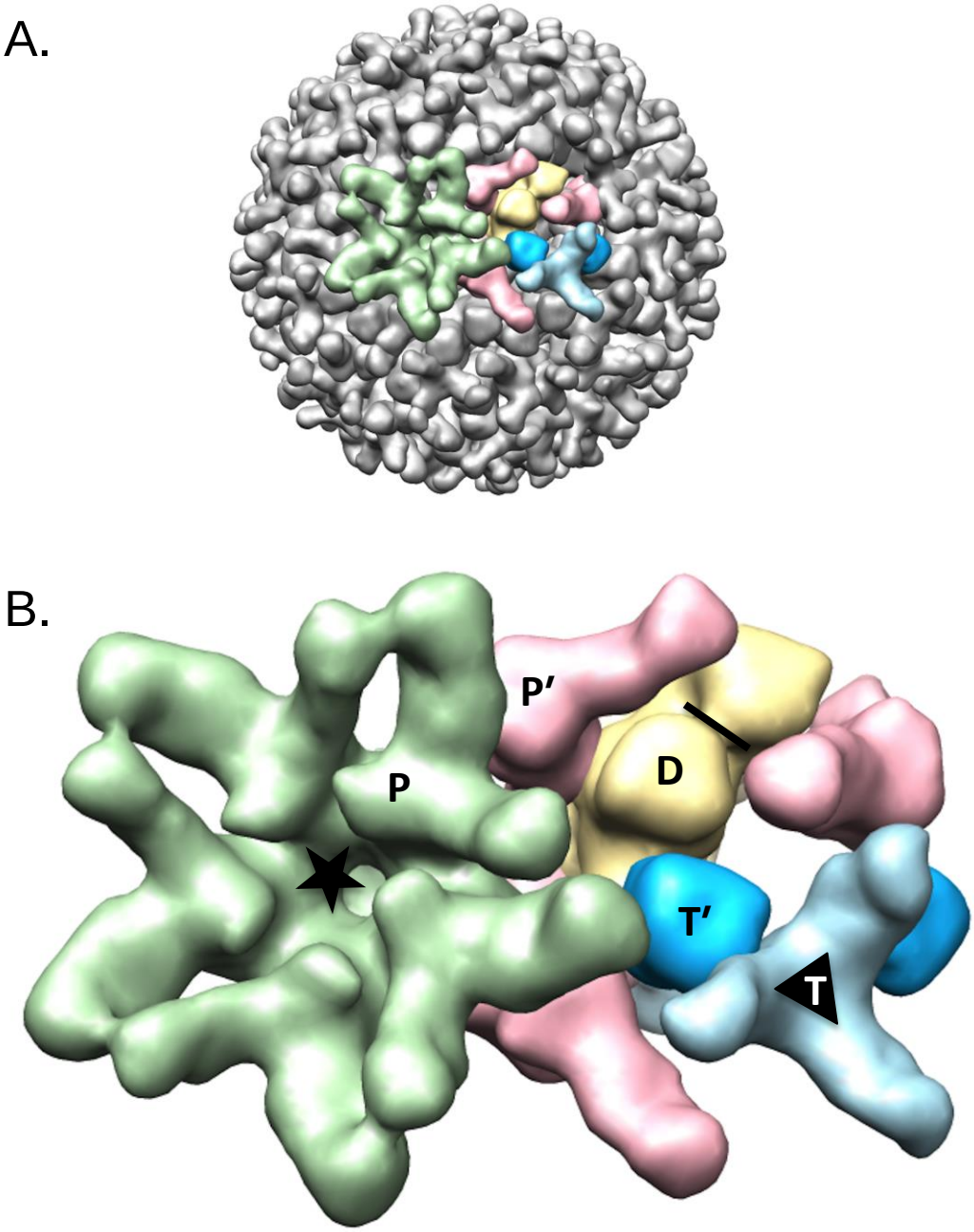

Figure 4-5. Binding of RV6-25 Fab all three channel types. (A) Surface representation of RV6-25-DLP complex particle, highlighting the RV6-25 Fabs bound to the VP6 trimers in the type I, II or III channel in the context of the whole virion particle (gray). (B) Representative arrangement of the RV6-25 Fabs bound to VP6 trimers in relation to adjacent Fabs bound to adjacent VP6 trimers. The trimers are labeled by color and position. The star and black line, triangle and star represent the two, three or five-fold axes of symmetry respectively.

Discussion

Previous work in our laboratory has characterized the two antibodies, RV6-25 and RV6-26, both members of the V_H1-46 immunodominant gene segment family that share the same germline sequence. However, while RV6-26 has inhibitory activity, RV6-25 does not (27). In chapter III, I determined the mechanism of antiviral activity of the RV6-26 antibody. It was of interest to investigate the structural basis of the lack of antiviral activity of RV6-25, since they share a common germline. This study of the cryo-EM structure, together with the DXMS studies, of the RV6-25-DLP complex reveals a different binding epitope for RV6-25. While RV6-26 was observed to bind directly into the transcription pore to access its quaternary epitope, almost resembling a plug that fits over the pore, RV6-25 binds on the apical loops of the VP6 trimers at a binding orientation of 45°. Even though Fab densities that project towards the transcription pore are observed, the binding orientation of the Fab densities is such that it can allow for extrusion of mRNA from an actively transcribing DLP. The Fabs do not appear to fit over the pore in such a way that it can act as a cap that will block mRNA extrusion. This observation can explain the basis of the lack of antiviral activity of RV6-25.

The cryo-EM structure of the RV6-25-DLP complex also revealed an interesting binding pattern of the RV6-25 Fab that informs on the overall structure of the RV-DLP. The prevalence of icosahedral particles adopted by viruses points to the genetic economy of viruses. A consequence of icosahedral packaging is that the subunits inevitably exhibit quasi-equivalence (11) or non-equivalence (13, 54) variations among the conformations and interactions of their arrayed subunits. Rotavirus exhibits a quasi-equivalent arrangement because of the symmetry mismatch between the VP2 and VP6

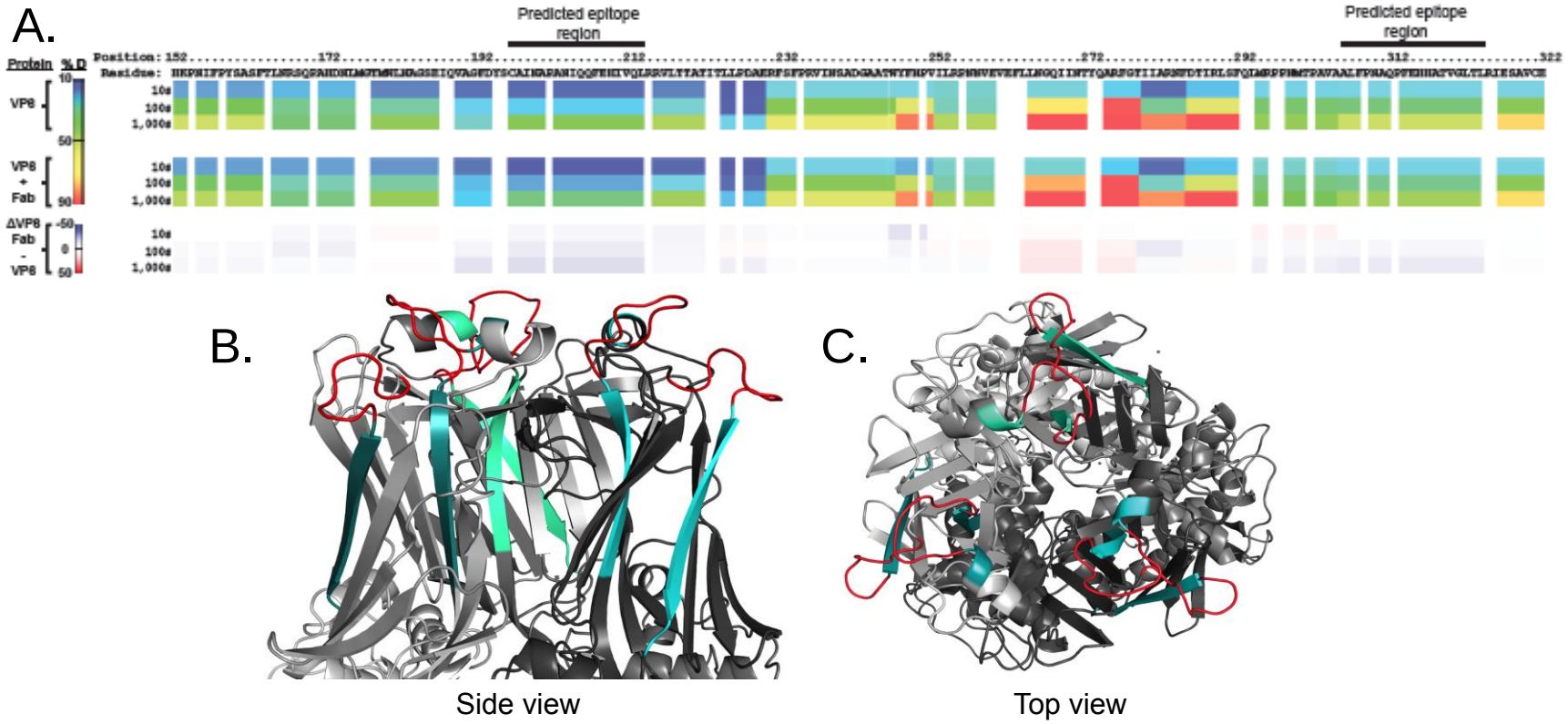

Figure 4-6. Determination of VP6 epitope for RV6-25 by deuterium exchange mass spectroscopy. Ribbon map showing percent deuterated (% D) of VP6 alone (A, top band), or VP6 bound to RV6-25 Fab (A, middle band). The top row shows the residue position number, the second row shows the residue and the rest of the rows show protein dynamic features at different on-exchange timepoints (10, 100, or 1,000 seconds [s]). As indicated in the colored bar, cold colors suggest relatively stable regions and warm colors suggest relatively flexible regions. All prolines are shown in white because prolines do not have amide hydrogens. Residues uncovered by surface deuteration are also shown in white. (A, bottom band). Difference map showing the influence of RV6-25 Fab binding to VP6 indicated by changes in % D. Blue suggests the regions that exchange slower upon Fab binding; red suggests the regions that exchange faster upon Fab binding. (B) Side view of the predicted epitope regions of RV6-25 Fab on the head domain of the VP6 structure (PDB: 1QHD). The different shades of gray represent the three protomers that make up the VP6 trimer, and the different shades of blue represent the predicted epitope regions mapped on each protomer, highlighting, in red, the loops that are most likely involved in binding to RV6-25. (C) The top view of the VP6 trimer with all the predicted epitope regions visible on the structure.

layers (43). The accompanying shifts are generally envisaged to be slight, but they can result in pronounced functional differences, as in the ability to bind other proteins. For example, three quasi-equivalent sites on tubular capsids of bacteriophage T4 were found to differ markedly in their affinities for the accessory protein *Soc* (3). Variations may also be expressed in antigenicity, and such differences have been observed between the penton and hexon forms of the major capsid protein of herpes simplex virus (68), and of cucumber mosaic virus (CMV) (7), and on L1, the major capsid protein of papillomavirus (6). Indeed, this property offers an additional mechanism for generating antigenic diversity on a viral capsid. The antibody investigated in the CMV study (7) could discriminate between A, B and C subunits of the capsid protein, by binding only to the A subunit closest to the five-fold axes. The selectivity of the CMV Fab could reflect structural differences in subunits arising from quasi-equivalence in the CMV T3 icosahedron, but that it is unlikely since the majority of the βH-βI loops containing the antibody epitopes adopt essentially identical structures. The only geometric constraints are dictated by the differences in pentameric and hexameric arrangements of the capsid subunits. Hence Fabs acquire specificity simply by virtue of the quaternary differences in subunit arrangement in pentons and hexons. The RV6-25 epitope lies in similar loops on the apical surface of the VP6 protein. It is therefore plausible that the binding pattern of RV6-25 Fab is driven by constraints imposed by the geometry of the type I, II or III channels in the DLP surface.

Variability in occupancy among quasi-equivalent forms of the same epitope appears to be quite common among viral antigens, as observed in the major capsid proteins of herpes simplex virus (68) and papillomavirus (6). The RV6-25 Fabs project off the epitope at the

corner of the VP6 trimer at an angle of about 45^{o}. This orientation allows the Fabs to extend out sideways over a relatively long distance, enlarging its footprint and blocking access to binding sites on neighboring trimers. The binding pattern of RV6-25 is likely a function of the combination of distinct environments around the DLP VP6 trimers and accessibility to epitopes influenced by steric clashes of the antibody.

Chapter summary

In chapters II and III, I focused on characterizing the interactions between the virus-inhibiting RV6-26 antibody, by determining its epitope and mechanism of action. In this chapter, I present data that characterizes the interaction between RV6-25, a viral binding but non-inhibiting antibody, and rotavirus. That RV6-25 binds an epitope on the apical edge of the transcription pore rather than an epitope within the pore indicates that the location of an antibody epitope plays a role in the ability of the antibody to mediate function. I showed that subtle differences exist in the display of capsid protein on viral surfaces. These differences should be noted in the design to vaccines based on virus-like particles, as capsid arrangements can influence epitope presentation and accessibility and thus can affect the host immune response. Indeed, the magnitude and quality of the immune responses generated by an engineered viral vector or designed immunogen is influenced by the structure and flexibility of the epitope, as well as the structural context and accessibility of the epitope (21, 50).

CHAPTER V

SUMMARY AND FUTURE DIRECTIONS

Thesis summary

The work presented in this dissertation was performed to gain a better understanding of rotavirus antigen-antibody interactions. We have previously characterized two rotavirus genetically related rotavirus antibodies, RV6-25 and RV6-26 that exhibited different binding and antiviral capacities. In this thesis, I determined the epitope of the two antibodies and elucidate the structural basis of their functional qualities.

I first attempted to determine the x-ray crystal structure of the antibody-VP6 complexes. To achieve this goal, we designed a VP6 construct that comprised of the residues that form the antibody-accessible portion of the VP6 antigen. I show data that demonstrate that our domain construct forms a trimeric stable structure that closely resembles the full-length VP6 protein. Our attempts to determine a co-crystal structure of the antibody-VP6 complex have so far been unsuccessful. However, we determined high-resolution crystal structures of the VP6 head domain construct and the inhibitory RV6-26 Fab. Next we used a biochemical technique, hydrogen-deuterium exchange mass spectrometry (DXMS), to determine the epitope and paratope of the RV6-26 antibody. These studies revealed that the RV6-26 epitope formed a quaternary structure, mainly spanning across the lateral surface of the VP6 trimer, involving adjacent subunits of the

VP6 trimer. This data suggested that in the context of the virion particle, RV6-26 likely binds within the pores of the viral surface.

Previous studies in our lab have demonstrated the inhibitory activity of the RV6-26 antibody. However, the mechanism of antiviral function was unknown. To determine the mechanism of antiviral function of the antibody, we used cryo-EM of RV6-26-DLP complexes to determine the structural basis of the inhibition. This work resulted in a relatively high-resolution complex structure that indicated that the mechanism of action was via physical blockade of the transcriptional pore. The computational modeling studies based on the quaternary nature of the epitope confirmed our initial findings. Published reports have shown that VP7 in the transcriptionally inactive TLP causes a conformational shift in the DLP layer that blocks RV transcription, and some have suggested a similar effect with bound anti-VP6 antibodies (12, 20, 33, 36, 66). We tested whether RV6-26 could induce the same conformational change, but found that it did not indeed induce such a change. I also show data from electrostatic analysis of the VP6hd and RV6-26 Fab surface that indicate that a strong electrostatic compatibility of the negatively charged epitope and positively charged paratope. Since the negatively charged surface of the VP6 trimer have been implicated to be involved in mRNA egress from the pore, this data suggest additional basis for the inhibitory effect of RV6-26.

Finally, since RV6-25 is closely related to RV6-26, but does not have antiviral activity, I investigated the structural basis for the lack of antiviral activity of the RV6-25 antibody by cryo-EM. We found that RV6-25 Fab binds to the apical edge of the VP6 trimer at the top of the transcription pore. The Fab does not appear to cover enough of the channel to completely seal it and block transcription as observed with RV6-26. These

data suggest the location of an epitope, in the context of a whole virus is important in mediating an antiviral effect. Furthermore, the cryo-EM structure of the RV6-25-DLP complex provided insights into quasi-equivalence nature of the VP6 trimers on the viral surface. Subtle differences in conformational environment and the molecular packing arrangement impacted the accessibility and hence occupancy of the VP6 epitopes. These observations have also been reported in other viruses such as CMV, HSV and papillomavirus.

Collectively, the work presented in this thesis provides a structural basis for the effective inhibition of rotavirus by an anti-VP6 antibody. Also structural information observed on the availability and display of viral capsid proteins have implications on the usage of icosahedral viruses, such as adenovirus, as vectors for display of epitopes in designing vaccines, as epitope accessibility will consequently affect the host immune response.

Future directions

This dissertation presents data that help define the structural basis of antiviral activity of anti-VP6 antibodies. However many questions remain unanswered about the role of anti-VP6 antibodies in human rotavirus immunity. Since the VP6 protein is only exposed when the virus is inside the cell, specific locations as to the site of interaction of VP6 and anti-VP6 antibodies remain elusive. Presumably, only VP6-specific IgAs will be able to gain access to rotavirus intracellular. Still, it is not clear how or where pIgA that transcytoses in the endosomal compartment from the basolateral to apical surface would bind to RV VP6 that is present in the cytoplasm. The majority of basolaterally

internalized IgA resides in the apical recycling endosome (ARE) (5). Preliminary co-localization studies using immunofluorescence and immunoelectron microscopy studies suggest that the interaction of pIgA and Sendai virus occurs near the apical plasma membrane in multi-lamellar structures that could be the ARE compartment (23). It is possible that RV-DLP encounters anti-VP6 IgAs at the AREs. An IgA molecular form of RV6-26 has already been synthesized in our laboratory and an intracellular neutralization assay has been established. Novel imaging techniques, such laser scanning confocal microscopy could be used to determine co-localization of IgAs and DLPs in AREs. Also a number of effector and motor proteins, including mysosin Vb and Rab11-FIP2, are involved in the trafficking of AREs. Inhibition of the function of these proteins and studying its effect on intracellular neutralization can yield insights into the localization of the VP6-antibody interaction within host cells.

An interesting observation resulting from this thesis work is the electrostatic compatibility of the highly inhibitory antibody with the VP6 negatively charged surface within the transcription pore. Given the implication of the importance of this surface to mRNA egress, it will be interesting to investigate whether the electrostatic interaction is an important driving force mediating the antiviral effect. The crystal structure of the VP6 protein has already been determined. Reverse genetics systems for the production of rotavirus have already been established (29). It is now possible to produce virus that have an altered electrostatic surface at that particular patch of residues that coincides with RV6-26 epitope. RV6-26 can then be tested to see if it retains its antiviral activity.

Finally, significant progress has been made towards the co-crystallization of RV6-26-VP6 and RV6-25-VP6. Crystals have been observed in initial crystallization trials of

RV6-26-VP6 and serve to reinforce efforts of determining high-resolution complex structures of VP6-anti-VP6 antibodies.

REFERENCES

1. Abbas, A. K., and A. H. Lichtman. 2003. Cellular and molecular immunology, 5th ed. Saunders, Philadelphia, PA.

2. Adams, P. D., R. W. Grosse-Kunstleve, L. W. Hung, T. R. Ioerger, A. J. McCoy, N. W. Moriarty, R. J. Read, J. C. Sacchettini, N. K. Sauter, and T. C. Terwilliger. 2002. PHENIX: building new software for automated crystallographic structure determination. Acta Crystallogr. Sect. D. Biol. Crystallogr. 58:1948-1954.

3. Aebi, U., R. van Driel, R. K. Bijlenga, B. ten Heggeler, R. van den Broek, A. C. Steven, and P. R. Smith. 1977. Capsid fine structure of T-even bacteriophages. Binding and localization of two dispensable capsid proteins into the P23* surface lattice. J. Mol. Biol. 110:687-698.

4. Aoki, S. T., E. C. Settembre, S. D. Trask, H. B. Greenberg, S. C. Harrison, and P. R. Dormitzer. 2009. Structure of rotavirus outer-layer protein VP7 bound with a neutralizing Fab. Science 324:1444-1447.

5. Apodaca, G., L. A. Katz, and K. E. Mostov. 1994. Receptor-mediated transcytosis of IgA in MDCK cells is via apical recycling endosomes. J. Cell Biol. 125:67-86.

6. Booy, F. P., R. B. Roden, H. L. Greenstone, J. T. Schiller, and B. L. Trus. 1998. Two antibodies that neutralize papillomavirus by different mechanisms show distinct binding patterns at 13 A resolution. J. Mol. Biol. 281:95-106.

7. Bowman, V. D., E. S. Chase, A. W. Franz, P. R. Chipman, X. Zhang, K. L. Perry, T. S. Baker, and T. J. Smith. 2002. An antibody to the putative aphid recognition site on cucumber mosaic virus recognizes pentons but not hexons. J. Virol. 76:12250-12258.

8. Brunger, A. T. 1997. Free R value: cross-validation in crystallography. Methods Enzymol. 277:366-396.

9. Brünger, A. T., P. D. Adams, and L. M. Rice. 1997. New applications of simulated annealing in X-ray crystallography and solution NMR. Structure 5:325-336.

10. Burns, J. W., M. Siadat-Pajouh, A. A. Krishnaney, and H. B. Greenberg. 1996. Protective effect of rotavirus VP6-specific IgA monoclonal antibodies that lack neutralizing activity. Science 272:104-107.

11. Caspar, D. L., and A. Klug. 1962. Physical principles in the construction of regular viruses. Cold Spring Harbor Symp. Quant. Biol. 27:1-24.

12. Chen, J. Z., E. C. Settembre, S. T. Aoki, X. Zhang, A. R. Bellamy, P. R. Dormitzer, S. C. Harrison, and N. Grigorieff. 2009. Molecular interactions in rotavirus assembly and uncoating seen by high-resolution cryo-EM. Proc. Natl. Acad. Sci. USA 106:10644-10648.

13. Cheng, R. H., V. S. Reddy, N. H. Olson, A. J. Fisher, T. S. Baker, and J. E. Johnson. 1994. Functional implications of quasi-equivalence in a T = 3 icosahedral animal virus established by cryo-electron microscopy and X-ray crystallography. Structure 2:271-282.

14. Diprose, J. M., J. N. Burroughs, G. C. Sutton, A. Goldsmith, P. Gouet, R. Malby, I. Overton, S. Zientara, P. P. C. Mertens, D. I. Stuart, and J. M. Grimes. 2001. Translocation portals for the substrates and products of a viral transcription complex: the bluetongue virus core. EMBO J. 20:7229-7239.

15. Durocher, Y., S. Perret, and A. Kamen. 2002. High-level and high-throughput recombinant protein production by transient transfection of suspension-growing human 293-EBNA1 cells. Nucleic Acids Res. 30:E9.

16. Emsley, P., and K. Cowtan. 2004. Coot: model-building tools for molecular graphics. Acta Crystallogr. Sect. D. Biol. Crystallogr. 60:2126-2132.

17. Estes, M. K. 2001. Rotavirus and their replication, p. 1747-1785. *In* D. M. Knipe and P. M. Howley (ed.), Fields Virology, vol. 2. Lippincott Williams and Wilkins, Philadelphia, PA.

18. Estes, M. K., and A. Z. Kapikian. 2007. Rotaviruses, p. 1918-1974. *In* D. M. Knipe and P. M. Howley (ed.), Fields Virology, vol. 2. Lippincott Williams and Wilkins, Philadelphia, PA.

19. Evans, P. 2006. Scaling and assessment of data quality. Acta Crystallogr. Sect. D. Biol. Crystallogr. 62:72-82.

20. Feng, N., J. A. Lawton, J. Gilbert, N. Kuklin, P. Vo, B. V. Prasad, and H. B. Greenberg. 2002. Inhibition of rotavirus replication by a non-neutralizing, rotavirus VP6-specific IgA mAb. J. Clin. Invest. 109:1203-1213.

21. Flatt, J. W., T. L. Fox, N. Makarova, J. L. Blackwell, I. P. Dmitriev, E. A. Kashentseva, D. T. Curiel, and P. L. Stewart. 2012. CryoEM visualization of an adenovirus capsid-incorporated HIV antigen. PLoS One 7:e49607.

22. Fleishman, S. J., A. Leaver-Fay, J. E. Corn, E. M. Strauch, S. D. Khare, N. Koga, J. Ashworth, P. Murphy, F. Richter, G. Lemmon, J. Meiler, and D. Baker. 2011. RosettaScripts: a scripting language interface to the Rosetta macromolecular modeling suite. PLoS One 6:e20161.

23. Fujioka, H., S. N. Emancipator, M. Aikawa, D. S. Huang, F. Blatnik, T. Karban, K. DeFife, and M. B. Mazanec. 1998. Immunocytochemical colocalization of

specific immunoglobulin A with sendai virus protein in infected polarized epithelium. J. Exp. Med. 188:1223-1229.

24. Hsu, S., Y. Kim, S. Li, E. S. Durrant, R. M. Pace, V. L. Woods, Jr., and M. S. Gentry. 2009. Structural insights into glucan phosphatase dynamics using amide hydrogen-deuterium exchange mass spectrometry. Biochemistry 48:9891-9902.

25. Kabsch, W. 2010. Integration, scaling, space-group assignment and post-refinement. Acta Crystallogr. Sect. D. Biol. Crystallogr. 66:133-144.

26. Kabsch, W. 2010. Xds. Acta Crystallogr. Sect. D. Biol. Crystallogr. 66:125-132.

27. Kallewaard, N. L., B. A. McKinney, Y. Gu, A. Chen, B. V. Prasad, and J. E. Crowe, Jr. 2008. Functional maturation of the human antibody response to rotavirus. J. Immunol. 180:3980-3989.

28. Kapikian, A. 2001. A rotavirus vaccine for prevention of severe diarrhoea of infants and young children: development, utilization and withdrawal. Novartis Found. Symp. 238:153-171. (Discussion, 238:171-179.).

29. Komoto, S., J. Sasaki, and K. Taniguchi. 2006. Reverse genetics system for introduction of site-specific mutations into the double-stranded RNA genome of infectious rotavirus. Proc Natl Acad Sci U S A 103:4646-4651.

30. Kostolansky, F., E. Vareckova, T. Betakova, V. Mucha, G. Russ, and S. A. Wharton. 2000. The strong positive correlation between effective affinity and infectivity neutralization of highly cross-reactive monoclonal antibody IIB4, which recognizes antigenic site B on influenza A virus haemagglutinin. J. Gen. Virol. 81:1727-1735.

31. Langedijk, J. P., N. K. Back, P. J. Durda, J. Goudsmit, and R. H. Meloen. 1991. Neutralizing activity of anti-peptide antibodies against the principal neutralization domain of human immunodeficiency virus type 1. J. Gen. Virol. 72 (Pt 10):2519-2526.

32. Lawton, J. A., M. K. Estes, and B. V. Prasad. 1999. Comparative structural analysis of transcriptionally competent and incompetent rotavirus-antibody complexes. Proc Natl Acad Sci U S A 96:5428-5433.

33. Lawton, J. A., M. K. Estes, and B. V. Prasad. 1999. Comparative structural analysis of transcriptionally competent and incompetent rotavirus-antibody complexes. Proc. Natl. Acad. Sci. USA 96:5428-5433.

34. Lawton, J. A., M. K. Estes, and B. V. Prasad. 2001. Identification and characterization of a transcription pause site in rotavirus. J Virol 75:1632-1642.

35. Lawton, J. A., M. K. Estes, and B. V. Prasad. 1997. Three-dimensional visualization of mRNA release from actively transcribing rotavirus particles. Nat Struct Biol 4:118-121.

36. Lawton, J. A., M. K. Estes, and B. V. Prasad. 1997. Three-dimensional visualization of mRNA release from actively transcribing rotavirus particles. Nat. Struct. Biol. 4:118-121.

37. Li, S., T. Tsalkova, M. A. White, F. C. Mei, T. Liu, D. Wang, V. L. Woods, Jr., and X. Cheng. 2011. Mechanism of intracellular cAMP sensor Epac2 activation: cAMP-induced conformational changes identified by amide hydrogen/deuterium exchange mass spectrometry (DXMS). J. Biol. Chem. 286:17889-17897.

38. Li, Z., M. L. Baker, W. Jiang, M. K. Estes, and B. V. Prasad. 2009. Rotavirus architecture at subnanometer resolution. J. Virol. 83:1754-1766.

39. Lovelace, E., H. Xu, C. A. Blish, R. Strong, and J. Overbaugh. 2011. The role of amino acid changes in the human immunodeficiency virus type 1 transmembrane domain in antibody binding and neutralization. Virology 421:235-244.

40. Lu, W. D., T. Liu, S. Li, V. L. Woods, Jr., and V. Hook. 2012. The prohormone proenkephalin possesses differential conformational features of subdomains revealed by rapid H-D exchange mass spectrometry. Protein Sci. 21:178-187.

41. Ludert, J. E., F. Gil, F. Liprandi, and J. Esparza. 1986. The structure of the rotavirus inner capsid studied by electron microscopy of chemically disrupted particles. J. Gen. Virol. 67 (Pt 8):1721-1725.

42. Mathieu, M., I. Petitpas, J. Navaza, J. Lepault, E. Kohli, P. Pothier, B. V. V. Prasad, J. Cohen, and F. A. Rey. 2001. Atomic structure of the major capsid protein of rotavirus: implications for the architecture of the virion. EMBO J. 20:1485-1497.

43. McClain, B., E. Settembre, B. R. Temple, A. R. Bellamy, and S. C. Harrison. 2010. X-ray crystal structure of the rotavirus inner capsid particle at 3.8 A resolution. J. Mol. Biol. 397:587-599.

44. McKinney, B. A., N. L. Kallewaard, J. E. Crowe, Jr., and J. Meiler. 2007. Using the natural evolution of a rotavirus-specific human monoclonal antibody to predict the complex topography of a viral antigenic site. Immunome Res. 3:8.

45. Offit, P. A., and G. Blavat. 1986. Identification of the two rotavirus genes determining neutralization specificities. J. Virol. 57:376-378.

46. Offit, P. A., G. Blavat, H. B. Greenberg, and H. F. Clark. 1986. Molecular basis of rotavirus virulence: role of gene segment 4. J. Virol. 57:46-49.

47. Otwinowski, Z., and W. Minor. 1997. Processing of X-ray diffraction data collected in oscillation mode. Methods Enzymol. Volume 276:307-326.

48. Painter, J., and E. A. Merritt. 2006. Optimal description of a protein structure in terms of multiple groups undergoing TLS motion. Acta Crystallogr. Sect. D. Biol. Crystallogr. 62:439-450.

49. Pettersen, E. F., T. D. Goddard, C. C. Huang, G. S. Couch, D. M. Greenblatt, E. C. Meng, and T. E. Ferrin. 2004. UCSF Chimera--a visualization system for exploratory research and analysis. J Comput Chem 25:1605-1612.

50. Plummer, E. M., and M. Manchester. 2010. Viral nanoparticles and virus-like particles: platforms for contemporary vaccine design. Wiley Interdiscip Rev Nanomed Nanobiotechnol.

51. Porta, C., G. Wang, H. Cheng, Z. Chen, T. S. Baker, and J. E. Johnson. 1994. Direct imaging of interactions between an icosahedral virus and conjugate F(ab) fragments by cryoelectron microscopy and X-ray crystallography. Virology 204:777-788.

52. Prasad, B. V., G. J. Wang, J. P. Clerx, and W. Chiu. 1988. Three-dimensional structure of rotavirus. J. Mol. Biol. 199:269-275.

53. Prasad, B. V. V., R. Rothnagel, C. Q. Y. Zeng, J. Jakana, J. A. Lawton, W. Chiu, and M. K. Estes. 1996. Visualization of ordered genomic RNA and localization of transcriptional complexes in rotavirus. Nature 382:471-473.

54. Rayment, I., T. S. Baker, D. L. Caspar, and W. T. Murakami. 1982. Polyoma virus capsid structure at 22.5 A resolution. Nature 295:110-115.

55. Roost, H. P., M. F. Bachmann, A. Haag, U. Kalinke, V. Pliska, H. Hengartner, and R. M. Zinkernagel. 1995. Early high-affinity neutralizing anti-viral IgG responses without further overall improvements of affinity. Proc Natl Acad Sci U S A 92:1257-1261.

56. Roseman, A. M., O. Borschukova, J. A. Berriman, S. A. Wynne, P. Pumpens, and R. A. Crowther. 2012. Structures of hepatitis B virus cores presenting a model epitope and their complexes with antibodies. J. Mol. Biol. 423:63-78.

57. Roseto, A., J. Escaig, E. Delain, J. Cohen, and R. Scherrer. 1979. Structure of rotaviruses as studied by the freeze-drying technique. Virology 98:471-475.

58. Rossmann, M. G., and J. E. Johnson. 1989. Icosahedral RNA virus structure. Annu. Rev. Biochem. 58:533-573.

59. Sauter, N. K., R. W. Grosse-Kunstleve, and P. D. Adams. 2004. Robust indexing for automatic data collection. J. Appl. Crystallogr. 37:399-409.

60. Schrodinger, LLC. 2010. The PyMOL Molecular Graphics System, Version 1.3r1.

61. Shaw, A. L., R. Rothnagel, D. Chen, R. F. Ramig, W. Chiu, and B. V. V. Prasad. 1993. Three-dimensional visualization of the rotavirus hemagglutinin structure. Cell 74:693-701.

62. Shaw, A. R. 2006. The rotavirus vaccine saga. Annu Rev Med 57:167-180.

63. Shibata, J., K. Yoshimura, A. Honda, A. Koito, T. Murakami, and S. Matsushita. 2007. Impact of V2 mutations on escape from a potent neutralizing anti-V3 monoclonal antibody during in vitro selection of a primary human immunodeficiency virus type 1 isolate. J. Virol. 81:3757-3768.

64. Steckbeck, J. D., I. Orlov, A. Chow, H. Grieser, K. Miller, J. Bruno, J. E. Robinson, R. C. Montelaro, and K. S. Cole. 2005. Kinetic rates of antibody binding correlate with neutralization sensitivity of variant simian immunodeficiency virus strains. J Virol 79:12311-12320.

65. Thouvenin, E., S. Laurent, M. F. Madelaine, D. Rasschaert, J. F. Vautherot, and E. A. Hewat. 1997. Bivalent binding of a neutralising antibody to a calicivirus involves the torsional flexibility of the antibody hinge. J. Mol. Biol. 270:238-246.

66. Thouvenin, E., G. Schoehn, F. Rey, I. Petitpas, M. Mathieu, M. C. Vaney, J. Cohen, E. Kohli, P. Pothier, and E. Hewat. 2001. Antibody inhibition of the transcriptase activity of the rotavirus DLP: a structural view. J. Mol. Biol. 307:161-172.

67. Toran, J. L., L. Sanchez-Pulido, L. Kremer, G. del Real, A. Valencia, and A. C. Martinez. 2001. Improvement in affinity and HIV-1 neutralization by somatic mutation in the heavy chain first complementarity-determining region of antibodies triggered by HIV-1 infection. Eur J Immunol 31:128-137.

68. Trus, B. L., W. W. Newcomb, F. P. Booy, J. C. Brown, and A. C. Steven. 1992. Distinct monoclonal antibodies separately label the hexons or the pentons of herpes simplex virus capsid. Proc Natl Acad Sci U S A 89:11508-11512.

69. Vagin, A., and A. Teplyakov. 1997. MOLREP: an automated program for molecular replacement. J. Appl. Crystallogr. 30:1022-1025.

70. Weitkamp, J. H., N. Kallewaard, K. Kusuhara, E. Bures, J. V. Williams, B. LaFleur, H. B. Greenberg, and J. E. Crowe, Jr. 2003. Infant and adult human B cell responses to rotavirus share common immunodominant variable gene repertoires. J. Immunol. 171:4680-4688.

71. Weitkamp, J. H., N. L. Kallewaard, A. L. Bowen, B. J. Lafleur, H. B. Greenberg, and J. E. Crowe, Jr. 2005. VH1-46 is the dominant immunoglobulin heavy chain

gene segment in rotavirus-specific memory B cells expressing the intestinal homing receptor alpha4beta7. J. Immunol. 174:3454-3460.

72. Weitkamp, J. H., B. J. Lafleur, and J. E. Crowe, Jr. 2006. Rotavirus-specific CD5+ B cells in young children exhibit a distinct antibody repertoire compared with CD5- B cells. Hum. Immunol. 67:33-42.

73. Weitkamp, J. H., B. J. Lafleur, H. B. Greenberg, and J. E. Crowe, Jr. 2005. Natural evolution of a human virus-specific antibody gene repertoire by somatic hypermutation requires both hotspot-directed and randomly-directed processes. Hum. Immunol. 66:666-676.

74. Winter, G. 2010. xia2: an expert system for macromolecular crystallography data reduction. J. Appl. Crystallogr. 43:186-190.

75. Yeager, M., J. A. Berriman, T. S. Baker, and A. R. Bellamy. 1994. Three-dimensional structure of the rotavirus haemagglutinin VP4 by cryo-electron microscopy and difference map analysis. EMBO J. 13:1011-1018.

76. Yeager, M., K. A. Dryden, N. H. Olson, H. B. Greenberg, and T. S. Baker. 1990. Three-dimensional structure of rhesus rotavirus by cryoelectron microscopy and image reconstruction. J. Cell Biol. 110:2133-2144.

77. Yoshiyama, H., H. Mo, J. P. Moore, and D. D. Ho. 1994. Characterization of mutants of human immunodeficiency virus type 1 that have escaped neutralization by a monoclonal antibody to the gp120 V2 loop. J. Virol. 68:974-978.

78. Zhang, X., E. Settembre, C. Xu, P. R. Dormitzer, R. Bellamy, S. C. Harrison, and N. Grigorieff. 2008. Near-atomic resolution using electron cryomicroscopy and single-particle reconstruction. Proc. Natl. Acad. Sci. USA 105:1867-1872.

79. Zhang, X., E. Settembre, C. Xu, P. R. Dormitzer, R. Bellamy, S. C. Harrison, and N. Grigorieff. 2008. Near-atomic resolution using electron cryomicroscopy and single-particle reconstruction. Proc Natl Acad Sci U S A 105:1867-1872.

80. Zhang, Z., and D. L. Smith. 1993. Determination of amide hydrogen exchange by mass spectrometry: a new tool for protein structure elucidation. Protein Sci. 2:522-531.